Calhoun: The NPS Institutional Archive

DSpace Repository

Theses and Dissertations | 1. Thesis and Dissertation Collection, all items

2014-12

MEMS-based waste vibration and acoustic energy harvesters

Householder, Timothy J.

Monterey, California: Naval Postgraduate School

http://hdl.handle.net/10945/44583

This publication is a work of the U.S. Government as defined in Title 17, United States Code, Section 101. Copyright protection is not available for this work in the United States.

Downloaded from NPS Archive: Calhoun

http://www.nps.edu/library

Calhoun is the Naval Postgraduate School's public access digital repository for research materials and institutional publications created by the NPS community. Calhoun is named for Professor of Mathematics Guy K. Calhoun, NPS's first appointed -- and published -- scholarly author.

Dudley Knox Library / Naval Postgraduate School
411 Dyer Road / 1 University Circle
Monterey, California USA 93943

NAVAL POSTGRADUATE SCHOOL

MONTEREY, CALIFORNIA

THESIS

MEMS-BASED WASTE VIBRATION AND ACOUSTIC ENERGY HARVESTERS

by

Timothy J. Householder

December 2014

Thesis Advisor: Dragoslav Grbovic
Co-Advisor: Bruce Denardo

Approved for public release; distribution is unlimited

THIS PAGE INTENTIONALLY LEFT BLANK

REPORT DOCUMENTATION PAGE

Form Approved OMB No. 0704–0188

Public reporting burden for this collection of information is estimated to average 1 hour per response, including the time for reviewing instruction, searching existing data sources, gathering and maintaining the data needed, and completing and reviewing the collection of information. Send comments regarding this burden estimate or any other aspect of this collection of information, including suggestions for reducing this burden, to Washington headquarters Services, Directorate for Information Operations and Reports, 1215 Jefferson Davis Highway, Suite 1204, Arlington, VA 22202-4302, and to the Office of Management and Budget, Paperwork Reduction Project (0704-0188) Washington, DC 20503.

1. AGENCY USE ONLY *(Leave blank)*	**2. REPORT DATE** December 2014	**3. REPORT TYPE AND DATES COVERED** Master's Thesis

4. TITLE AND SUBTITLE
MEMS-BASED WASTE VIBRATION AND ACOUSTIC ENERGY HARVESTERS

5. FUNDING NUMBERS

6. AUTHOR(S) Timothy J. Householder

7. PERFORMING ORGANIZATION NAME(S) AND ADDRESS(ES)
Naval Postgraduate School
Monterey, CA 93943-5000

8. PERFORMING ORGANIZATION REPORT NUMBER

9. SPONSORING /MONITORING AGENCY NAME(S) AND ADDRESS(ES)
N/A

10. SPONSORING/MONITORING AGENCY REPORT NUMBER

11. SUPPLEMENTARY NOTES The views expressed in this thesis are those of the author and do not reflect the official policy or position of the Department of Defense or the U.S. Government. IRB Protocol number ____N/A____.

12a. DISTRIBUTION / AVAILABILITY STATEMENT
Approved for public release; distribution is unlimited

12b. DISTRIBUTION CODE
A

13. ABSTRACT (maximum 200 words)

Every machine vibrates and emits noise. This is unused energy that, with an appropriate mechanism, can be returned to the system. Utilizing an array of piezoelectric microelectromechanical systems (MEMS) devices to harvest this otherwise wasted energy, it is possible to improve the efficiency of any number of mechanical devices.

Piezoelectricity is the mechanism by which certain crystalline structures generate electric potential when under strain, or, conversely, deform when subjected to an electric potential. It is this first effect that is important to this application. Though each MEMS device will generate a very small amount of power, a 1 m^2 area can contain an array of millions of these devices.

Energy harvesting, conservation, and efficiency are all key Department of Defense (DOD) priorities, and the universal application of these devices make them ideal for any expeditionary platform, such as ships, aircraft, and automobiles.

This thesis designs and tests the first generations of acoustic and vibrational piezoelectric MEMS devices; including time-dependent finite element models, microfabrication processes, and the initial attempts at characterization and optimization.

14. SUBJECT TERMS
MEMS, energy harvesting, piezoelectric, resonator

15. NUMBER OF PAGES
89

16. PRICE CODE

17. SECURITY CLASSIFICATION OF REPORT	**18. SECURITY CLASSIFICATION OF THIS PAGE**	**19. SECURITY CLASSIFICATION OF ABSTRACT**	**20. LIMITATION OF ABSTRACT**
Unclassified	Unclassified	Unclassified	UU

NSN 7540–01-280-5500

Standard Form 298 (Rev. 2–89)
Prescribed by ANSI Std. 239–18

THIS PAGE INTENTIONALLY LEFT BLANK

Approved for public release; distribution is unlimited

MEMS-BASED WASTE VIBRATION AND ACOUSTIC ENERGY HARVESTERS

Timothy J. Householder
Lieutenant Commander, United States Navy
B.S., University of Idaho, 2002

Submitted in partial fulfillment of the
requirements for the degree of

MASTER OF SCIENCE IN PHYSICS

from the

NAVAL POSTGRADUATE SCHOOL
December 2014

Author: Timothy J. Householder

Approved by: Dragoslav Grbovic
Thesis Advisor

Bruce Denardo
Co-Advisor

Andres Larraza
Chair, Department of Physics

THIS PAGE INTENTIONALLY LEFT BLANK

ABSTRACT

Every machine vibrates and emits noise. This is unused energy that, with an appropriate mechanism, can be returned to the system. Utilizing an array of piezoelectric microelectromechanical systems (MEMS) devices to harvest this otherwise wasted energy, it is possible to improve the efficiency of any number of mechanical devices.

Piezoelectricity is the mechanism by which certain crystalline structures generate electric potential when under strain, or, conversely, deform when subjected to an electric potential. It is this first effect that is important to this application. Though each MEMS device will generate a very small amount of power, a 1 m^2 area can contain an array of millions of these devices.

Energy harvesting, conservation, and efficiency are all key Department of Defense (DOD) priorities, and the universal application of these devices makes them ideal for any expeditionary platform, such as ships, aircraft, and automobiles.

This thesis designs and tests the first generations of acoustic and vibrational piezoelectric MEMS devices; including time-dependent finite element models, microfabrication processes, and the initial attempts at characterization and optimization.

THIS PAGE INTENTIONALLY LEFT BLANK

TABLE OF CONTENTS

I. INTRODUCTION....1
A. BACKGROUND....1
B. SCOPE OF THESIS....2

II. PHYSICS WITHIN THE DESIGN....3
A. MICROELECTROMECHANICAL SYSTEMS....3
B. PIEZOELECTRIC EFFECT....3
1. Theory....3
2. Energy Conversion and Resonance Frequency....4
C. GENERATING ELECTRICAL CURRENT....6

III. MATERIALS SELECTION AND ANALYSIS....9
A. ALUMINUM NITRIDE....9
B. BIMATERIAL....10
C. SUBSTRATE....10
D. DEVICE ANALYSIS....10

IV. DESIGN....11
A. SUSPENDED, MULTIFOLD MICROBRIDGE DESIGN....11
B. GENERAL DIMENSIONS AND THEIR IMPLICATIONS....12
C. SPECIFIC DESIGNS....12
1. Design 1: PiezoMUMPs Fabrication....13
2. Design 2: NPS Fabrication with SOI....14
3. Design 3: NPS Fabrication with SU-8....15

V. MICROFABRICATION PROCESS....17
A. GENERAL....17
1. Sputter Deposition of AlN....17
B. INDIVIDUAL MICROFABRICATION SEQUENCE....21

VI. MATERIAL AND DEVICE CHARACTERIZATION....25
A. ELECTRON MICROSCOPY....25
B. PHYSICAL AND OPTICAL MEASUREMENTS....26
C. LAYER THICKNESS....29
D. NANOINDENTER (YOUNG'S MODULUS)....29

VII. EXPERIMENTAL RESULTS....33
A. OUTPUT VOLTAGE MEASUREMENTS....33
1. Acoustic Measurements....33
a. Response to Varying Incident Amplitude....36
b. Modal Analysis....37
c. Unusual Data....43
d. Lorentzian Curve-Fitting....44
2. Mechanical Measurements....46
a. Output Voltage....47
b. Modal Analysis....48

c. Lorentzian Curve-Fitting *49*
3. Comparison of Acoustic and Mechanical Actuation 52
B. ESTIMATE OF DAMPING PARAMETERS 57
C. COMPARISON OF SIMULATION AND MEASUREMENTS 58
1. Eigenfrequency 58
2. Damping 59
D. ESTIMATE OF POWER AND EFFICIENCY 60
VIII. FUTURE WORK 63
A. MODELING 63
1. Exploring the Parameter Space 63
2. Next Generation Devices 63
B. FABRICATION 64
1. NPS Fabrication with SOI and SU-8 64
a. Fabrication *64*
b. SU-8 Analysis *64*
2. NPS Deposition of AlN 64
C. TESTING 65
1. Conditioning Circuit 65
2. Multiple Device Arrays 65
3. Power and Efficiency Analysis 65
4. Failure Analysis 65
5. Investigating Unusual Findings 66
D. MODAL ANALYSIS 66
1. Center-Pad versus Anchor-Point Actuation 66
2. Helmholtz Resonance 66
LIST OF REFERENCES 67
INITIAL DISTRIBUTION LIST 71

LIST OF FIGURES

Figure 1. Computer-generated finite-element model of a piezoelectric device, showing stress magnitude by color during deformation. 4
Figure 2. *LRC* circuit model of a piezoelectric device. 5
Figure 3. Time-dependent electrical power output of device across varying load, driven at 0.1 mm displacement, from [1]. 7
Figure 4. a) SEM and b) XRD of c-axis oriented thin-film AlN, from [1]. 9
Figure 5. PiezoMUMPs generations. Note the bridges attached to the corners of the center pad in the third generation device. 14
Figure 6. Graphic of the mask for a 6-legged piezoelectric energy harvester, annotated with structure notes and dimensions, from [1]. The device is grey, the substrate is light blue, and the trench is white. 15
Figure 7. MEMSPro images of SU-8 designs, 1- to 8-legged structures. 16
Figure 8. Atomic spectroscopy comparison of sputtering with varying Ar/N_2 blends. 18
Figure 9. Sputtering of Al target to Si substrate with a) 100%, b) 50%, and c) 0% N_2. 19
Figure 10. Atomic spectroscopy of sputtered Al_2O_3/AlN using 100% N_2. 19
Figure 11. SEM image of sputtered Al_2O_3/AlN. 20
Figure 12. Whole wafer after attempted AlN deposition at Naval Postgraduate School. 21
Figure 13. The Naval Postgraduate School microfabrication. Silicon is shown in grey. SiO2 is shown in green. AlN is shown in blue, from [1]. 22
Figure 14. SEM images of second generation PiezoMUMPs device. 26
Figure 15. Optical profilometer image of NPS fabricated on SOI device. 27
Figure 16. Optical profilometer measurements of device. The curvature of the center pad and legs is expected and is due to residual stress from the microfabrication process. (Note: scale is exaggerated in z direction). 28
Figure 17. Ten nanoindentations of AlN film. 30
Figure 18. NanoIndenter results for Young's modulus of silicon, 9 of 10 tests. E_{Si} = 173.3 GPa, SE_{Si} = 0.8 GPa. 31
Figure 19. NanoIndenter results for Young's modulus of aluminum nitride, 22 of 24 tests. E_{AlN} = 384.0 GPa, SE_{AlN} = 3.8 GPa. 32
Figure 20. Acoustic test apparatus. 34
Figure 21. Acoustic trials, average of 10 sweeps over multiple days, 100 Hz to 1 kHz. 35
Figure 22. Response and impedance curves for HL14-25 horn, from [26]. 35
Figure 23. Linear output variation with input gain adjustment. 36
Figure 24. Optical microscope image of PiezoMUMPs third generation device, showing laser vibrometer data locations. Each leg is 250 μm wide. 37
Figure 25. Acoustic trials. Note varying resonance peaks at 220 Hz, 525 Hz, 710 Hz, and 755 Hz and different relative sizes based on location of measurement.

The top graph is at full scale to show the 220 Hz peak, the bottom graph is scaled to emphasize the higher-frequency peaks. 38
Figure 26. COMSOL deformation shapes for modes at a) 229 Hz and b) 259 Hz, corresponding to c) acoustic peaks observed at 207 Hz and 223 Hz, respectively. Note the corners measure higher than the leg, and the center measures disproportionately higher near 207 Hz....40
Figure 27. a) COMSOL deformation shape for mode at 579 Hz, corresponding to b) acoustic peak observed at 526 Hz. Note the leg measures highest, the corners somewhat in the middle, and the center barely deflects at all....41
Figure 28. COMSOL deformation shapes for modes at a) 710 Hz and b) 840 Hz, corresponding to c) acoustic peaks observed at 702 Hz and 751 Hz, respectively. Note the leg measures highest, the corners do not deflect at 710 Hz, corner 1 measures higher than corner 2 at 751 Hz, and the center barely deflects at all. 42
Figure 29. Lorentzian curves fit to acoustically-actuated experimental data averaged over all points (top) and only at the leg (bottom). The top graph in each set is at full scale to show the 220 Hz peak, the bottom graph in each set is scaled to emphasize the higher-frequency peaks. 45
Figure 30. Vibrational test apparatus. 47
Figure 31. High speed camera still image of device. 47
Figure 32. Vibrational sweeps from 200 Hz to 900 Hz, normalized to accelerometer output. 48
Figure 33. COMSOL mechanically-actuated mode shapes at a) 366 Hz, b) 504 Hz, c) 661 Hz, and d) 800 Hz. 49
Figure 34. Comparison of scaled LIA data, Oscilloscope data, and best-fit Lorentzian at 380 Hz (top); showing phase shift on LIA (bottom)....50
Figure 35. Acceleration performance of shaker under various test loads, from [29]. 51
Figure 36. Amplitude response for accelerometer, from [30]. 51
Figure 37. Mechanical excitation in the acoustic experimental set-up. The top graph is at full scale to show the 220 Hz peak, the bottom graph is scaled to emphasize the higher-frequency peaks. 53
Figure 38. Comparison of mechanical actuation in the mechanical and acoustic experimental set-ups. The measuring point in the acoustic set-up is the device's legs and has been smoothed for clarity of comparison. 54
Figure 39. COMSOL acoustically-actuated mode shapes at a) 229 Hz, b) 259 Hz, c) 579 Hz, d) 710 Hz, and e) 840 Hz. 55
Figure 40. COMSOL mechanically-actuated mode shapes at a) 366 Hz, b) 504 Hz, c) 661 Hz, and d) 800 Hz. 55
Figure 41. Lorentzian curves fit to vibrationally-actuated experimental data. 56
Figure 42. COMSOL frequency domain sweep 200 Hz - 900 Hz for center-pad (top) and anchor-point (bottom) actuation, in increments of 1 Hz, using the above damping parameters. 59

LIST OF TABLES

Table 1. Summary of attempted reactive sputtering 10nm AlN, with varying Ar/N_2 blend. 18
Table 2. Atomic composition of sputtered Al_2O_3/AlN. 20
Table 3. Device thickness. 29
Table 4. Summary of Lorentzian Fit-to-Leg parameters and modal analysis, with relative displacement color-coded to match COMSOL display. 46
Table 5. Summary of fit Lorentzian parameters. 57
Table 6. Lorentzian parameters used to fit initial Rayleigh damping parameters, taken from the Lorentzian curve fitting of the acoustic data. 58
Table 7. Eigenfrequencies generated by finite element modeling. 59
Table 8. Summary of COMSOL input parameters. 60
Table 9. Power delivered by one device. 61

THIS PAGE INTENTIONALLY LEFT BLANK

LIST OF ACRONYMS AND ABBREVIATIONS

AC	Alternating current
Al_2O_3	Alumina (Aluminum Oxide)
AlN	Aluminum Nitride
Ar	Argon gas
DOD	Department of Defense
E_n	Young's modulus of material n
FWHM	Full Width at Half Maximum
LIA	Lock-In Amplifier
MEMS	Microelectromechanical System
ν_n	Poisson's ratio of material n
N_2	Nitrogen gas
NPS	Naval Postgraduate School
Q	Quality Factor
SEM	Scanning Electron Microscope
SE	Standard Error
Si	Silicon
SiO_2	Silicon Dioxide
SOI	Silicon on Insulator
SPR	A positive photoresist, manufactured by Dow
SU-8	A negative photoresist, manufactured by MicroChem
V_{p-p}	Peak-to-peak voltage
V_{rms}	Root mean square voltage
XRD	X-ray diffraction

THIS PAGE INTENTIONALLY LEFT BLANK

ACKNOWLEDGMENTS

Though I cannot name everyone who helped make this possible, I would like to express my deep and sincere gratitude to the following people:

Of course, I would like to thank my advisors, Professors Drago Grbovic and Bruce Denardo, without whom this thesis would be of embarrassingly poor quality.

Many Naval Postgraduate School professors taught me how to gather and interpret this data. I would like to thank the professors in the Physics Department; especially Professors Fabio Alves, Nancy Haegel, Jim Luscombe, Steve Baker, and Gamani Karunasiri; as well as all of the professors who taught me enough physics to become dangerous, like Professors Brett Borden, Joseph Hooper, Pete Crooker, Joe Blau, Sebastian Osswald, Kevin Smith, Dick Harkins, Daphne Kapolka, Scott Davis, and Richard Olsen.

I had far more help than I probably deserved from those outside the Physics Department, like Professors Claudia Luhrs, Sarath Menon, Luke Brewer, and Emily Craparo.

I would not have been able to take any data without the help of the Physics Department staff, especially Alex Fuhrmann, Sam Barone, Gene Morris, Steven Jacobs, and Eric Malycha.

Finally, and most importantly, I would like to thank my family. Without the patience and encouragement of my wife, Jaime, especially these last few weeks, I would have lost all my hair by now.

THIS PAGE INTENTIONALLY LEFT BLANK

I. INTRODUCTION

This thesis continues the work started by former Naval Postgraduate students Sarah Gregory and Daniel Hogue in which the first generations of vibrational and acoustic energy-harvesting piezoelectric MEMS devices were modeled using finite element modeling software, and the initial fabrication steps were developed [1]. Energy harvesting devices can have a wide range of designs and functions. This thesis investigates piezoelectric MEMS-based double-ended multifold cantilevers.

A. BACKGROUND

Developing a sustainable fleet is at the forefront of much of the Department of the Navy's strategic planning. Not only is a petroleum-dependent fleet expensive and environmentally burdensome, it also demands the strategic vulnerability of relying on other nations' petroleum exports.

Sustainable energy is among the most important issues to the current administration [2], and the Department of Defense and its components have been directed "to increase military effectiveness and mitigate cost, develop more energy-efficient weapons systems, platforms, equipment, and facilities capable of utilizing multiple energy sources; invest in cost-effective energy sources (including alternative energy); and promote non-materiel and behavior-based solutions" [3]. Waste energy harvesting is identified as a key science and technology objective in the 2012 U.S. Marine Corps S&T Strategic Plan [4], and MEMS energy-harvesting devices can lighten the logistical burden required by USMC and Navy expeditionary units.

The development and widespread use of vibrational and acoustic harvesting MEMS would aid the effort to meet each of these goals in the Department of the Navy by contributing to the overall energy portfolio and decreasing the necessity for use of petroleum-based generators for production of electricity by improving their overall efficiency.

B. SCOPE OF THESIS

Piezoelectricity is the mechanism by which certain crystalline structures generate electric potential when under strain; or, conversely, deform when subjected to an electric potential. Simulations performed by Gregory and Hogue [1] show it is possible to harvest waste energy to power small electronic devices by developing a piezoelectric microelectromechanical system.

This thesis is primarily focused on the completion of the microfabrication steps initially developed by Gregory, characterization of the completed devices, and feedback of the obtained parameters (previously unavailable) into the finite-element modeling simulations conducted by Hogue in order to obtain a more accurate model. Other avenues of investigation include reactive ion sputtering of aluminum nitride (AlN) using an aluminum target with nitrogen gas, the use of SU-8 photoresist, vice silicon (Si), as a structural layer, and analyzing the effect of additional multifold legs on resonance frequencies, all in an effort to bring a complete microfabrication process to NPS.

The remaining microfabrication process steps have been completed to finish the device, as well as some process refinement. Experimental results have been fed back into the model developed in [1] in order to refine and optimize the model. These MEMS devices may be tuned for 60Hz or 50Hz to return waste energy from U.S. U.S. or foreign electrical distribution systems, or can be designed for a swath of resonance frequencies in order to design the devices for specific vibration instruments, or for bulk energy harvesting.

II. PHYSICS WITHIN THE DESIGN

Energy-harvesting devices can have a wide range of designs and functions. This chapter introduces MEMS and describes basic principles of piezoelectric energy harvesting devices.

A. MICROELECTROMECHANICAL SYSTEMS

Following closely behind the semiconductor-based integrated circuit industry, the MEMS field has capitalized upon the significant advances made in photolithography and Si-based microfabrication [5]. MEMS are in use today in many systems, such as motion-sensors in mobile phones and gaming devices, pressure sensors in automobile tires and airbags, and a multitude of small-scale devices such as microphones and infrared cameras.

Microelectromechanical systems, due to their small size and low cost, are ideal for bulk energy-harvesting applications. The dimensions of a typical MEMS device are on the order of microns, so one array can consist of millions, perhaps billions of MEMS devices. While each individual device may not provide much usable energy, an array of MEMS devices can have significant returns with a very small footprint.

B. PIEZOELECTRIC EFFECT

Piezoelectricity is highly scalable and can provide a very efficient means of energy conversion [6]. Because of this, piezoelectric devices have become prevalent in modern equipment, from flame lighters to MEMS devices to ultrasonic transceivers for material testing [7]. For a material to be piezoelectric it must be a noncentrosymmetric crystal; that is, it must have no center of symmetry.

1. Theory

When a stress (force per unit cross-sectional area) is applied to a noncentrosymmetric crystal in certain directions, it causes a strain (fractional change in length), which shifts the center of mass of the respective opposing ions. This shift can

create an electric dipole, which is not necessarily along the same direction as the applied stress.

If the piezoelectric coefficient is expressed as a matrix there is a linear relationship between the applied mechanical stress, T_j, and the induced polarization, P_i; as well as a linear relationship between the applied electric field E_i, and the induced strain, S_j. The indices i and j indicate direction, known as the "ij-mode." Many piezoelectric materials have more than one possible resonance mode, describing the difference between the directions of applied stress and polarization, which is determined by the crystalline geometry [7]. Note the piezoelectric coefficient d_{ij} is the same in both equations below, which is due to reciprocity:

$$\begin{aligned} P_i &= d_{ij} T_j \\ S_j &= d_{ij} E_i . \end{aligned} \tag{1}$$

Piezoelectrics, like all crystals, are frequently identified by their axes: a and b (horizontal) or c (vertical). Figure 1 shows stresses on the legs of a piezoelectric device.

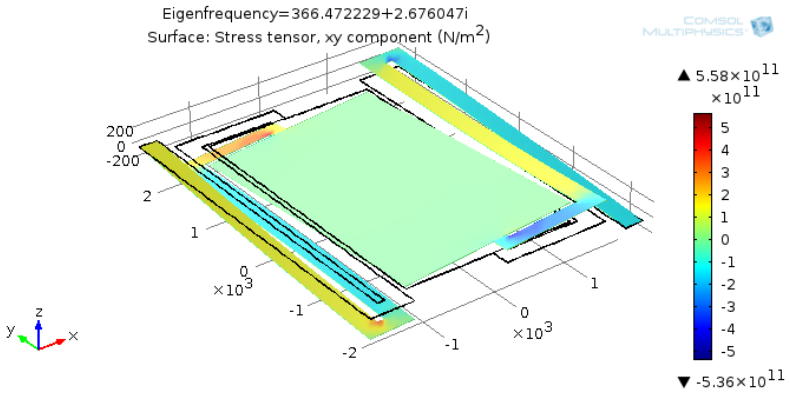

Figure 1. Computer-generated finite-element model of a piezoelectric device, showing stress magnitude by color during deformation.

2. Energy Conversion and Resonance Frequency

The effectiveness of the energy conversion process (not to be confused with the efficiency) can be described with an electromechanical coupling factor

$$k^2 = \frac{\text{Energy converted}}{\text{Energy input}}. \tag{2}$$

The piezoelectric portion of any circuit will oscillate and, due to its electromechanical coupling, can be modeled as an *LRC* "tank" circuit with the equivalent formula for resonance frequency. As shown in [6], a piezoelectric energy conversion device has an efficiency of:

$$\eta = \frac{\frac{1}{2}\left(\frac{k^2}{1-k^2}\right)}{\frac{1}{Q}+\frac{1}{2}\left(\frac{k^2}{1-k^2}\right)}, \tag{3}$$

where k^2 is the electromechanical coupling factor and Q is the quality factor. The basic assumptions used in this derivation are that the maximum efficiency will occur at resonance frequency [6], and that the device can be modeled as the equivalent circuit shown in Figure 2.

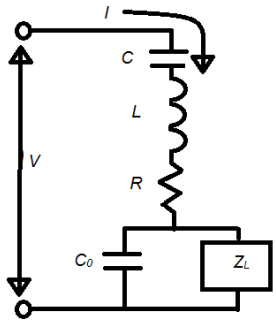

Figure 2. *LRC* circuit model of a piezoelectric device.

where L represents mass, C is stiffness, R is damping, and Z_L is the load in parallel with the piezoelectric device's electrodes. The resonance frequency is

$$f_s = \frac{1}{2\pi\sqrt{LC}}. \tag{4}$$

An unavoidable side effect of the physical use of such a device is the capacitance of the electrodes in parallel with the crystal, C_0. This causes an "antiresonance frequency."

$$f_a = \frac{1}{2\pi\sqrt{LC'}}, \tag{5}$$

where

$$\frac{1}{C'} = \frac{1}{C_0} + \frac{1}{C}. \tag{6}$$

Just as with any other *LRC* circuit, piezoelectric crystals have a quality factor Q that can be described in the same way [6]:

$$Q = \frac{1}{2\pi f_s RC}. \tag{7}$$

This analysis becomes ungainly when dealing with a more complicated design, or when analyzing an array of piezoelectric devices. This thesis uses finite-element-modeling software for in-depth analysis.

C. GENERATING ELECTRICAL CURRENT

Power is the rate of energy transfer, and in electrical systems is the product of current and voltage. In order for an energy-harvesting device to be useful it must have sufficient current capacity to deliver sufficient power to its load.

Piezoelectric devices can generate high electric potential differences (voltage); however, the current capacity of each device is severely limited. Finite element models from [1] suggest that an ideal load exists to which a single device can deliver the maximum power, as seen in Figure 3. This analysis will be addressed in Chapter VIII.

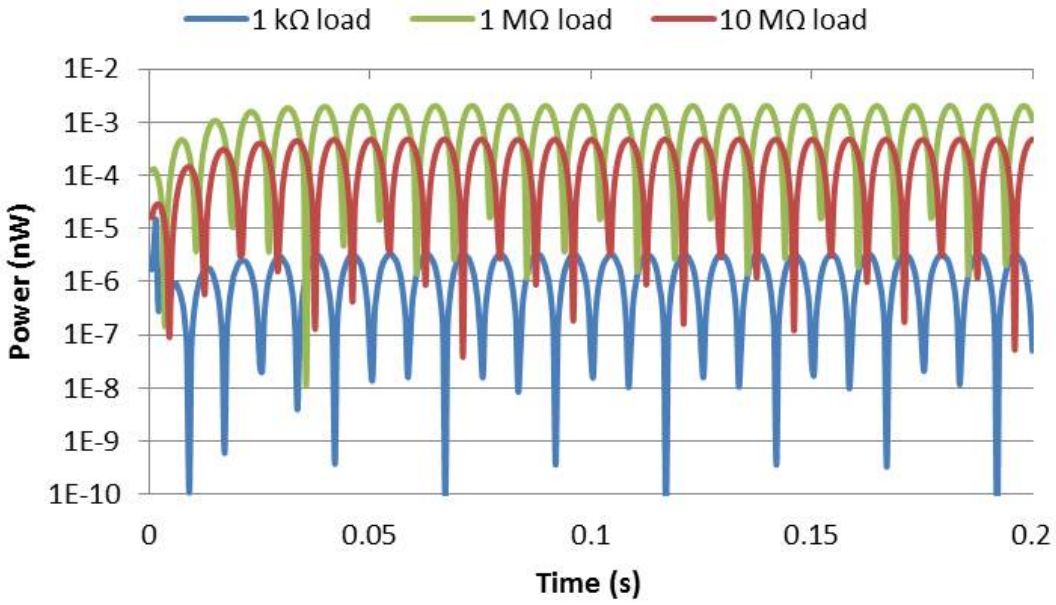

Figure 3. Time-dependent electrical power output of device across varying load, driven at 0.1 mm displacement, from [1].

Moreover, MEMS devices can be connected in series to step-up the voltage and in parallel to step-up the current capacity of the power-generating array. This analysis will be addressed in Chapter VIII.

THIS PAGE INTENTIONALLY LEFT BLANK

III. MATERIALS SELECTION AND ANALYSIS

The careful selection of materials is necessary to ensure an operational, reliable, and cost-effective device. This chapter describes this selection process and evaluates lower-cost alternatives.

A. ALUMINUM NITRIDE

Aluminum nitride is a common, inexpensive piezoelectric material with a high piezoelectric modulus; that is, sufficient potential is generated for a given strain. It is well suited to thin-film deposition and micromachining through wet etching, and is thus useful for MEMS applications.

The preferred modes of electromechanical coupling for AlN are the 33 (parallel) and 31 modes (perpendicular). For the purposes of this thesis a highly c-axis oriented AlN layer that excites the 31 mode is preferred [1]. There are two basic ways to determine orientation: examining morphology with a scanning electron microscope (SEM), and analyzing X-ray (Bragg) diffraction (XRD), as shown in Figure 4.

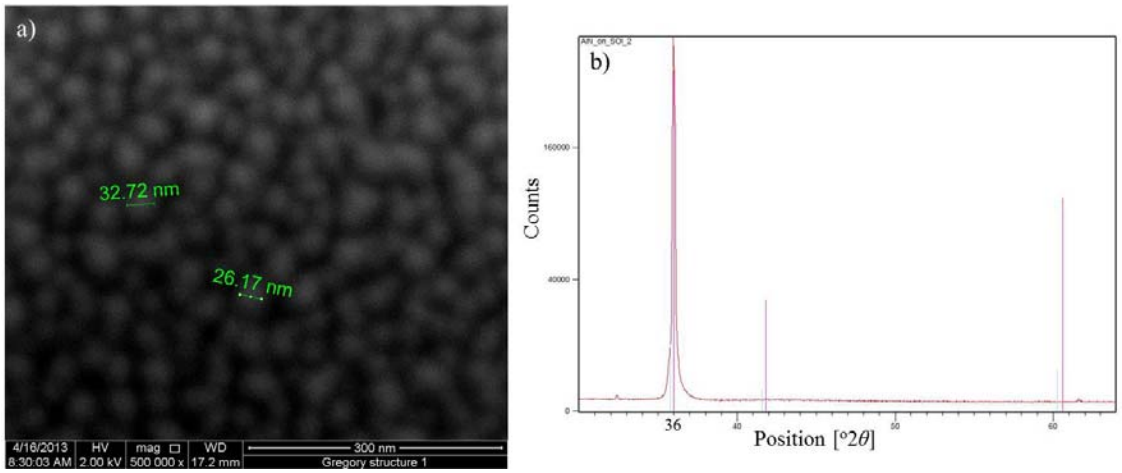

Figure 4. a) SEM and b) XRD of c-axis oriented thin-film AlN, from [1].

B. BIMATERIAL

Finite Element Modeling shows that a thin-film piezoelectric layer can generate a greater potential difference; however, this can lead to a structurally unsound device. A structure layer is necessary in order to have a device that can oscillate without failure. Silicon, due to its relative abundance and affordability, is among the most common materials used for this purpose.

C. SUBSTRATE

Due to their relative abundance and common use in CMOS circuits, we use Si substrates. The most effective, and most expensive, is Silicon-on-insulator (SOI). Other designs use deposited layers atop a bare silicon wafer.

SOI wafers typically have a 400 μm–600 μm Si substrate with a thin layer (0.5–10 μm) of silicon oxide (SiO_2) between the substrate and the surface layer of 1 μm–20 μm Si. This layout easily lends itself to the use of Si as a structure layer.

Other materials are being investigated for use as a structure layer, including aluminum and SU-8 Photoresist. The completion of this investigation is left for future work (see Section VIII.B).

D. DEVICE ANALYSIS

The finite-element-modeling software COMSOL is used to perform computer analysis of our design prior to fabrication. The physical device is tested and the experimental results are fed back into the computer model. This revises the given parameters to modify and update computer models to more accurately reflect reality. After sufficient accuracy of the model is achieved, multiple iterations of new generations of the energy harvesting devices can be optimized and designed without the need for time-consuming and costly microfabrication and characterization. This will lead to the ability to microfabricate highly optimized devices. This iterative process is left for future work (see Chapter VIII).

IV. DESIGN

There are several competing priorities for design criteria. The structure must be robust enough to withstand cyclic loading with pressures and displacements seen in real-world applications. A U.S. Navy gas turbine generator can vibrate up to 6 thousandths of an inch, or 150 μm, before alarming [8]. At its ideal operating speed of 3600 RPM, a vibrational energy harvesting device must withstand several billions of cycles each year without failure.

The device must have a resonance frequency that is low enough for real-world applications. For use with U.S. electrical generators this frequency is 60 Hz, for multinational generators it is 50 Hz (see paragraph II.B.2).

The device must also have good electrical properties: it must induce a high electric potential, and have a high current capacity (see sections II.B and II.C).

A. SUSPENDED, MULTIFOLD MICROBRIDGE DESIGN

MEMS devices tend to have resonance frequencies in the kHz and MHz ranges, though most useful applications are in the Hz ranges. The fundamental mode resonance frequency for a MEMS double-ended cantilever device with a central point load F can be approximated with

$$f_1 = \frac{13.86}{2\pi}\sqrt{\frac{EIg}{Fl^3}}, \tag{8}$$

and

$$I = \frac{wt^3}{12}, \tag{9}$$

where I is the moment of inertia, E is Young's modulus, g is the acceleration of gravity near the surface of the earth, and l, w, & t are the device's length, width, and thickness, respectively [5]. In order to design a device with a resonance frequency in usable ranges, the device must be long and thin, with a majority of its mass in the center. The most

compact possible geometry is used: long, multifold legs (providing large effective length) with a massive center pad.

B. GENERAL DIMENSIONS AND THEIR IMPLICATIONS

The highest electric potential will be induced at the point of the greatest stress, as shown in Equation (1). The point of greatest stress will also be the most susceptible to failure.

The device legs must be thick enough and wide enough to compensate for the longer legs and withstand the repetitive cyclic stresses of vibration without suffering failure or early fatigue. For a double-ended cantilever (fixed-fixed beam) the maximum stress will occur in the middle of each leg, which can be modeled as a fixed-free beam under point loading, as follows:

$$\theta = \frac{Fl^2}{2EI}, \tag{10}$$

where θ is the deflection angle, which correlates to stress [5]. Note the similarity to Equation (8). A low l or high t is desired to reduce the maximum stress felt by the cantilever structure. This is in direct conflict with the requirements for a low resonance frequency and a high induced electrical potential.

C. SPECIFIC DESIGNS

This thesis covers multiple lines of investigation, each using a different design. The design used in [1] is awaiting Deep Reactive Ion Etching, its final fabrication step, prior to experimental analysis. A set of similar designs was used to develop an ad-hoc formula for resonance frequency vs. cantilever leg length, specifically with regard to the number of folds in the multifold legs; these designs are also intended to be used in the examination of Al and of SU-8 as potential structure layers. The continued analysis of these designs is left for future work (see Chapter VIII).

Finally, a more robust design was developed for fabrication by a third-party commercial foundry, MEMSCap [1, 9]. A new method of fabricating piezoelectric MEMS devices, known as PiezoMUMPs, is under development and this thesis provides

some data to help characterize the PiezoMUMPs process [1]. The experimental data in Chapter VII come from the PiezoMUMPs devices.

Each design was modeled with COMSOL and designed using MEMS design software called MEMSPro.

1. Design 1: PiezoMUMPs Fabrication

The first generation PiezoMUMPs design in [1] did not survive shipping and thus could not be tested. The process itself was not the problem: the final step of cleaving the wafer into separate die while on sticky tape prior to shipping was where this issue occurred. The maximum displacement of the center pad would exceed the substrate thickness and stick to the shipping tape. During the attempted removal of the device from the shipping tape, the center pad (along with most of the legs) would remain affixed and shear off. Additionally, both electrode tabs tapped off the top of the legs and thus would not have obtained the optimum electric potential generated from the top to the bottom of the device.

The second generation device was designed with thicker legs to reduce the maximum displacement of the center pad, and with electrode pads placed to obtain the optimal "top-to-bottom" electric potential. The tradeoff with this design is a higher theoretical resonance frequency. The center pad continued to stick to the shipping tape.

The third generation device is more robust device with fewer legs; connected at the midpoint, rather than the corner, of the center pad; and with temporary "bridges" at the corners that pin the center pad to the substrate during shipping (Figure 5). This device has a higher theoretical resonance frequency than the two previous generations.

These three PiezoMUMPs generations are shown in Figure 5.

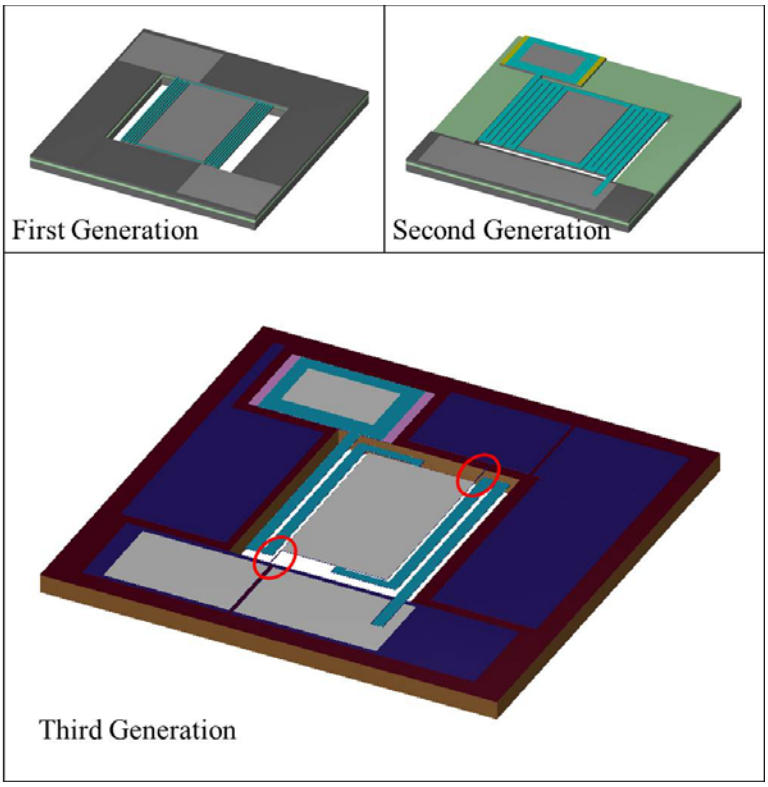

Figure 5. PiezoMUMPs generations. Note the bridges attached to the corners of the center pad in the third generation device.

2. Design 2: NPS Fabrication with SOI

There have been no changes to the designs for NPS fabrication used in [1]. This design will test 2-, 4-, and 6-legged structures. Figure 6 shows the dimensions of the 6-legged structure on the photolithography mask, generated with MEMSPro, of this device.

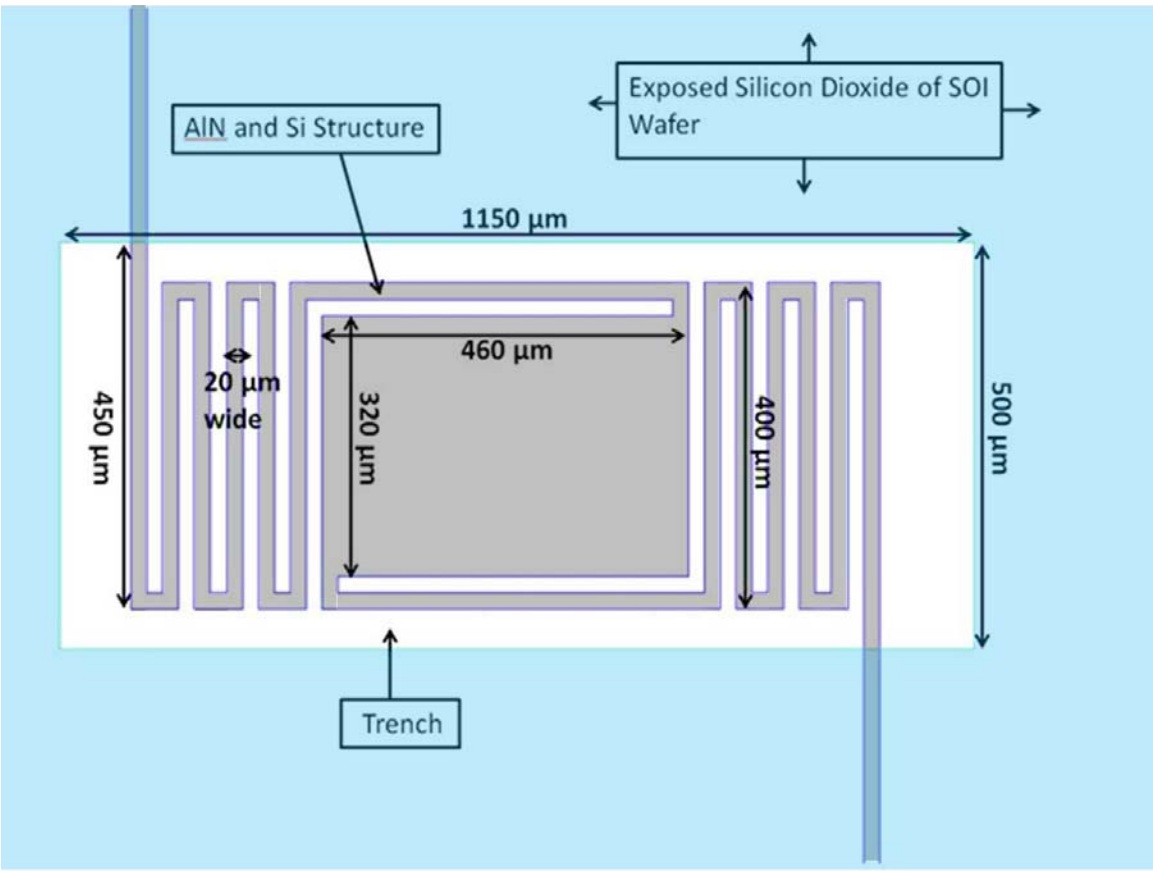

Figure 6. Graphic of the mask for a 6-legged piezoelectric energy harvester, annotated with structure notes and dimensions, from [1]. The device is grey, the substrate is light blue, and the trench is white.

This design uses SOI wafers which, though more costly, enable full production at NPS. Since the pre-fabricated SOI wafer already contains the structure layer, only two photolithography masks are required for complete microfabrication, the piezo/structure mask, and the backside (trench) mask. This process will be described in Chapter V. Due to the higher cost of SOI wafers (5–7 times the price of a bare silicon wafer), however, alternative structure materials, such as SU-8 and aluminum, are also being investigated.

3. Design 3: NPS Fabrication with SU-8

If structurally viable, SU-8 has some beneficial characteristics: it is quite inexpensive and it can be deposited quickly and easily via spin-coating in any laboratory. Due to its low Young's modulus (as low as 2 GPa [10] and as high as 5 GPa [11]) lower resonance frequencies and greater stress to the piezo layer can be achieved at much

smaller device size than would be possible with silicon-based devices, allowing for more dense packing and thus a larger number of devices per unit area.

Two separate wafer designs have been prepared to test SU-8 as a structure layer. Design 2: NPS Fabrication with SOI is used for a known comparison, and the second design will test the frequency response of SU-8 over a larger range of leg length, identified by the number of folds per side, as shown in Figure 7.

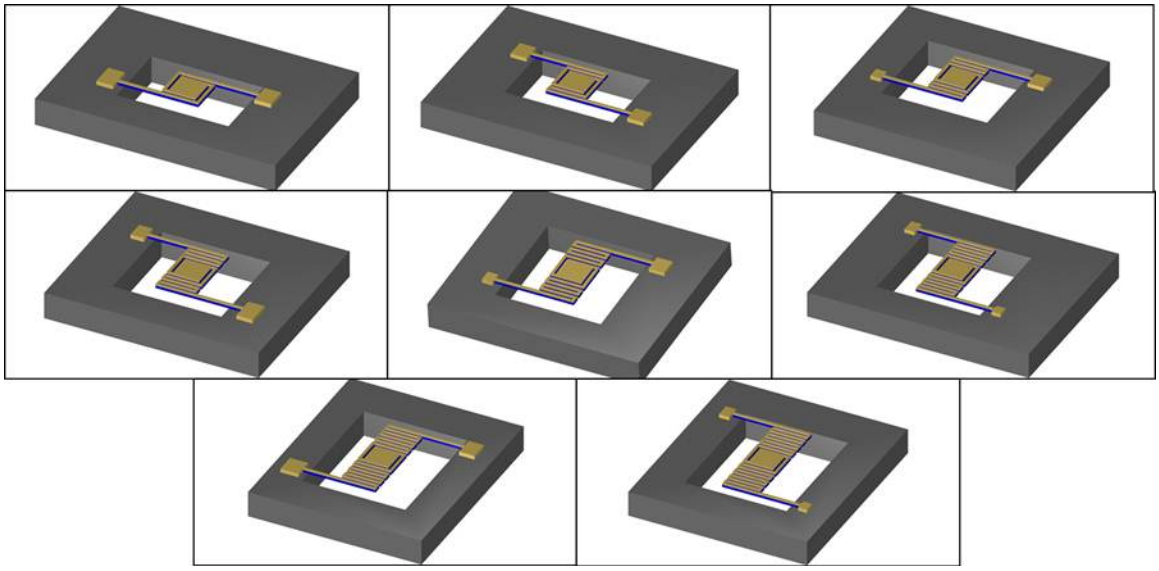

Figure 7. MEMSPro images of SU-8 designs, 1- to 8-legged structures.

Since the piezo layer is deposited directly atop the structure layer, only two photolithographic masks are required for complete microfabrication, just as with Design 2: NPS Fabrication with SOI. This process will also be described in Chapter V. These processes can be greatly simplified by expanding AlN reactive sputtering capabilities at NPS.

V. MICROFABRICATION PROCESS

As explained in Chapter IV, there were multiple microfabrication techniques evaluated. This chapter describes refinement of the NPS microfabrication process.

A. GENERAL

1. Sputter Deposition of AlN

Sputter deposition of AlN using facilities at NPS proved difficult. The instrument is intended to coat thin films of just a few nanometers for electron microscopy, and this capability did not scale to deposition thicknesses of several hundreds of nanometers onto a 4-inch wafer. The instrument was also not designed for use with more than one gas, intended to be argon. Finally, the sputter coater at NPS did not have any temperature control.

Initial attempts to sputter AlN onto a Si substrate examined varying ratios of argon (Ar) and nitrogen (N_2) gas, using a Cressington Sputter Coater 208HR. Literature shows better c-axis orientation using higher temperature, lower pressure, more power, and greater percentage of N_2 in the Ar/N_2 blend. The only tradeoff was in the Ar/N_2 blend: more Ar meant faster sputtering and less residual stress [12–19]. Different Ar/N_2 blends were tested on each of four samples taken from the same Si wafer. A 99.99% pure Al target was used for all reactive sputtering. Table 1 summarizes the experimental parameters, and Figure 8 shows the atomic spectroscopy results.

Table 1. Summary of attempted reactive sputtering 10nm AlN, with varying Ar/N_2 blend.

Sample #	$N_2/(N_2\text{-}Ar)$ [%]	Chamber Pressure [mBarr]	Sputter Current [mA]
1	Control	(Not	Sputtered)
2	0	0.02 ±0.01	78 ±2
3	100	0.03 ±0.01	76 ±2
4	50	0.02 ±0.01	76 ±3

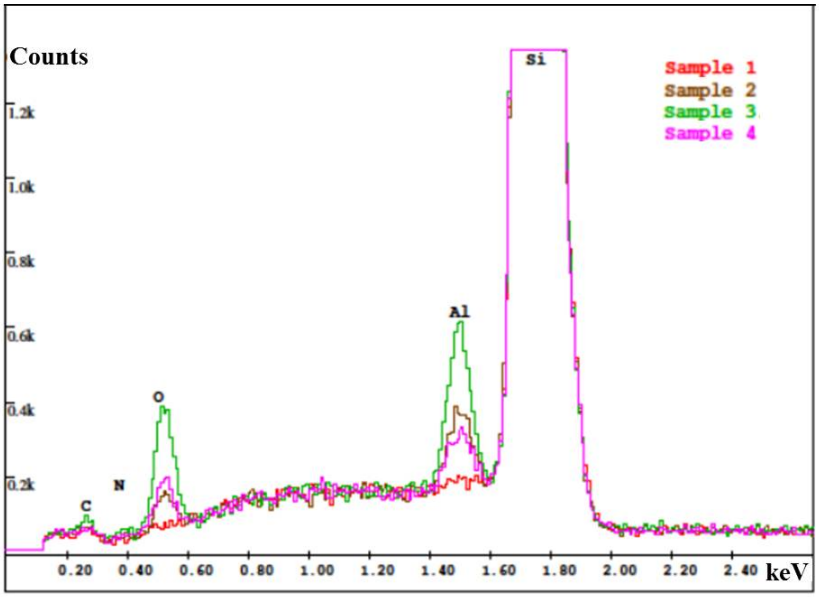

Figure 8. Atomic spectroscopy comparison of sputtering with varying Ar/N_2 blends.

The plasma color indicates the amount of Ar and N_2, as seen in Figure 9. The presence of oxygen also appeared to provide a more reddish hue.

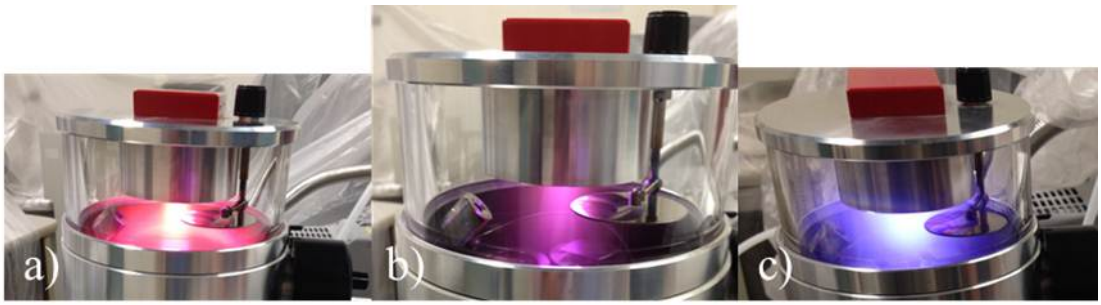

Figure 9. Sputtering of Al target to Si substrate with a) 100%, b) 50%, and c) 0% N_2.

Figure 10 shows atomic spectroscopy of an attempted deposition of AlN using 100% N_2 with a full Si wafer substrate. The high concentration of oxygen indicates that alumina (Al_2O_3) was preferentially deposited, followed by a roughly equivalent layer of AlN.

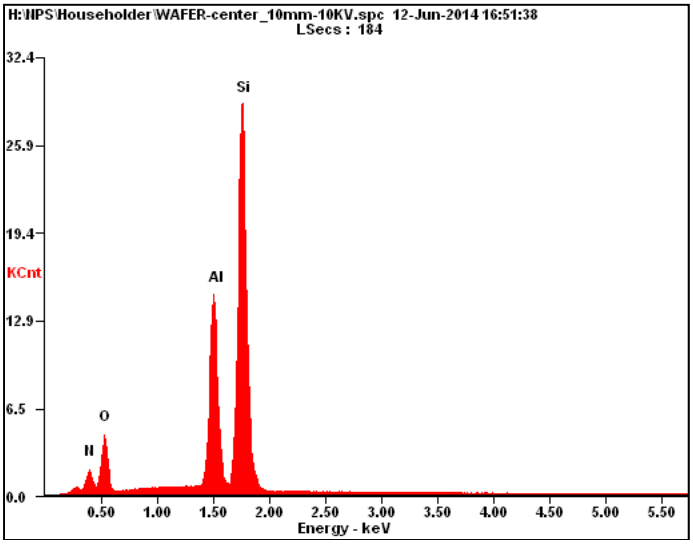

Figure 10. Atomic spectroscopy of sputtered Al_2O_3/AlN using 100% N_2.

Depending on crystalline orientation, the Si substrate has a native oxide layer approximately 1 nm thick [20], and the Al target has a native oxide layer approximately 5 nm thick [21]. Table 2 shows roughly equal concentrations by number of oxygen and nitrogen, indicating growth of both Al_2O_3 and AlN.

Table 2. Atomic composition of sputtered Al_2O_3/AlN.

Element	Wt%	At%
N	08.68	14.88
O	09.65	14.48
Al	23.34	20.77
Si	58.33	49.87

The morphological properties in Figure 11 appear very similar to AlN and show the desired "pebble type" c-axis orientation. These data are consistent with an initial deposition layer of Al_2O_3 on top of the natural SiO_2 layer; then, when sufficient oxygen inventory is reduced, AlN is deposited on top.

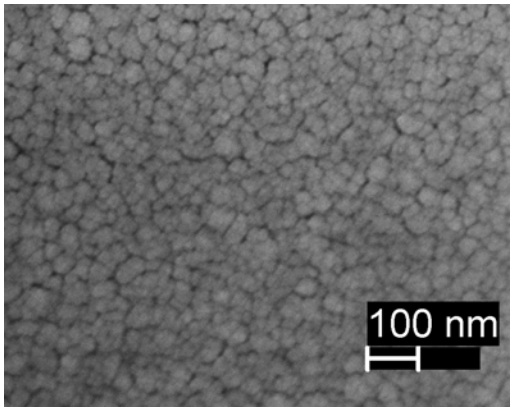

Figure 11. SEM image of sputtered Al_2O_3/AlN.

Filmetrics measurements show a roughly Gaussian distribution of sputtered layer thickness atop a 10-cm wafer, varying from approximately 90 nm at the edges to 200 nm in the center. The concentric rings in Figure 12 indicate the non-uniform deposition thickness.

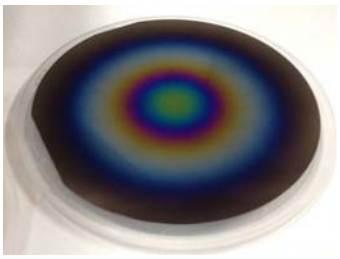

Figure 12. Whole wafer after attempted AlN deposition at Naval Postgraduate School.

B. INDIVIDUAL MICROFABRICATION SEQUENCE

This thesis further explores the NPS fabrication. These steps were developed in [1] and are listed again here, with some clarification and updates, for continuity:

> Fabrication begins with an SOI wafer, a section of which is shown in Figure 13a. Then, fabrication materials are deposited and etched in the following order:
>
> 1. AlN is deposited by AC powered S-gun magnetron for AlN reactive sputtering, as shown in Figure 13b.
>
> 2. The wafer is primed by spinning the wafer at 3000 RPM under several milliliters of MCC Primer, an organic solvent solution, to prepare the wafer for photoresist application.
>
> 3. 7 microns of SPR 220 photoresist are spin-coated on the primed wafer at 3000 RPM for 45 s. The wafer is then soft baked at 115°C for 90 s.
>
> 4. Next, the photoresist is exposed under the mask described in Chapter IV.C.2 at between 240 and 250 Integra, with a print gap of 30 microns.
>
> 5. The wafer rests for 30 minutes to allow for more solvent in the photoresist to evaporate. After at least 30 minutes, the wafer is post-exposure baked at 115°C for 90 s.
>
> 6. Photoresist is developed for 1 minute in CD-26 developer, to remove exposed photoresist.
>
> 7. The AlN is isotropically etched, using 85% H3PO4 at 85°C for 60–74 s, as shown in Figure 13c.
>
> 8. Using the AlN as a mask, a reactive ion etch will remove the top layer of Si, defining the structure, as shown in Figure 13d.

9. The top AlN and Si structures are protected by spinning the wafer surface with SPR 220–7, and then baking for four hours at 90°C [20].

10. The bottom side of the wafer is primed, as it was in step 2. Next, it is spin coated with SPR 220–7 under the same conditions in step 3.

11. The trench mask is aligned, using a backside aligner, which is available at Stanford Nanofabrication Facility at Stanford University.

12. Expose the wafer at 220 Integra, with a print gap of 30 microns. Develop for 3 minutes in CD-20. The result is shown in Figure 13e.

13. Etch the trench through the bottom Si layer using deep reactive ion etcher.

14. Remove the photoresist from the bottom layer, by soaking in acetone for 5 minutes and rinsing with isopropanol.

15. Use reactive ion etch on the SiO2 to complete the trench and release the energy harvesting structure, as shown in Figure 13f.

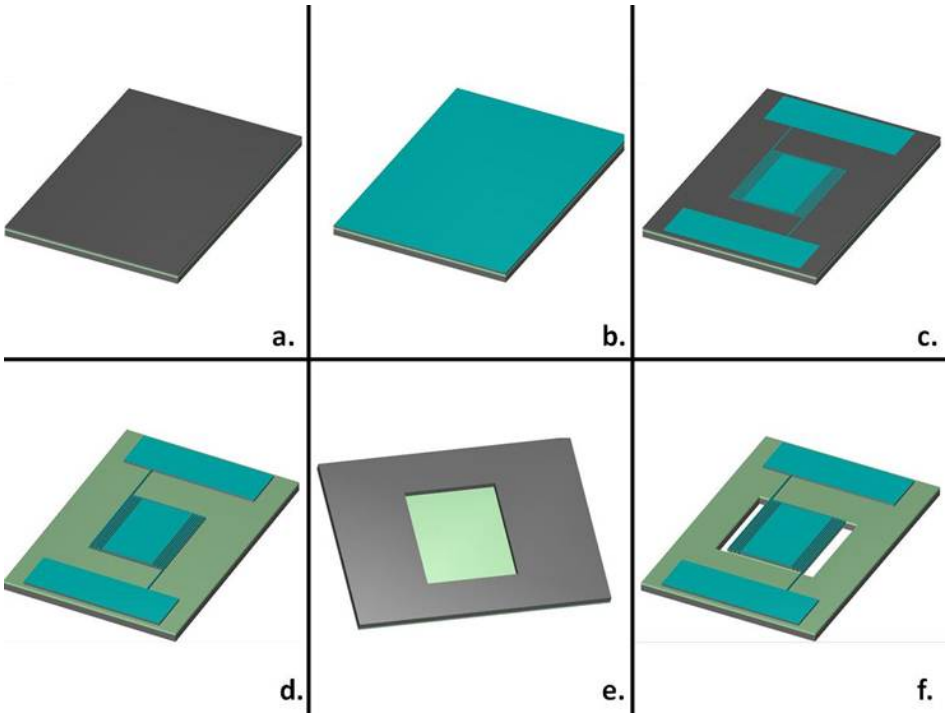

Figure 13. The Naval Postgraduate School microfabrication. Silicon is shown in grey. SiO_2 is shown in green. AlN is shown in blue, from [1].

The following additional steps to create an SU-8 structure layer occur prior to step 1, above.

1. Starting with a bare Si wafer, 500 nm of SU-8 is spin-coated at 3000 RPM and then softbaked for 60 seconds at 95^{o}C.

2. The SU-8 is exposed without a mask at 595 integra, then post-exposure baked for 120 seconds at 95^{o}C, and finally hardbaked for 30 minutes at 250^{o}C.

The wafer is then treated like an SOI wafer for the purposes of the above procedure without the need for step 15.

THIS PAGE INTENTIONALLY LEFT BLANK

VI. MATERIAL AND DEVICE CHARACTERIZATION

Characterization of each wafer and each device occurred with the Scanning Electron Microscope, and with the various devices in the Clean Room.

A. ELECTRON MICROSCOPY

SEM images were taken at various locations on the second generation PiezoMUMPs device. The first image in Figure 14 shows the entire device with the center pad and three legs stuck to the packing tape. Each image shows lateral separation between the Si structure layer and the AlN piezo layer. Images of the center pad also show lateral separation between the AlN piezo layer and the Al pad layer. The even horizontal striations on the structure layer are indicative of the deep reactive ion etching (also called BOSCH) process and the slight irregularities on the piezo and pad layers are indicative of wet etching [22]. Note the c-axis orientation of the AlN shown at the top of the second image from a).

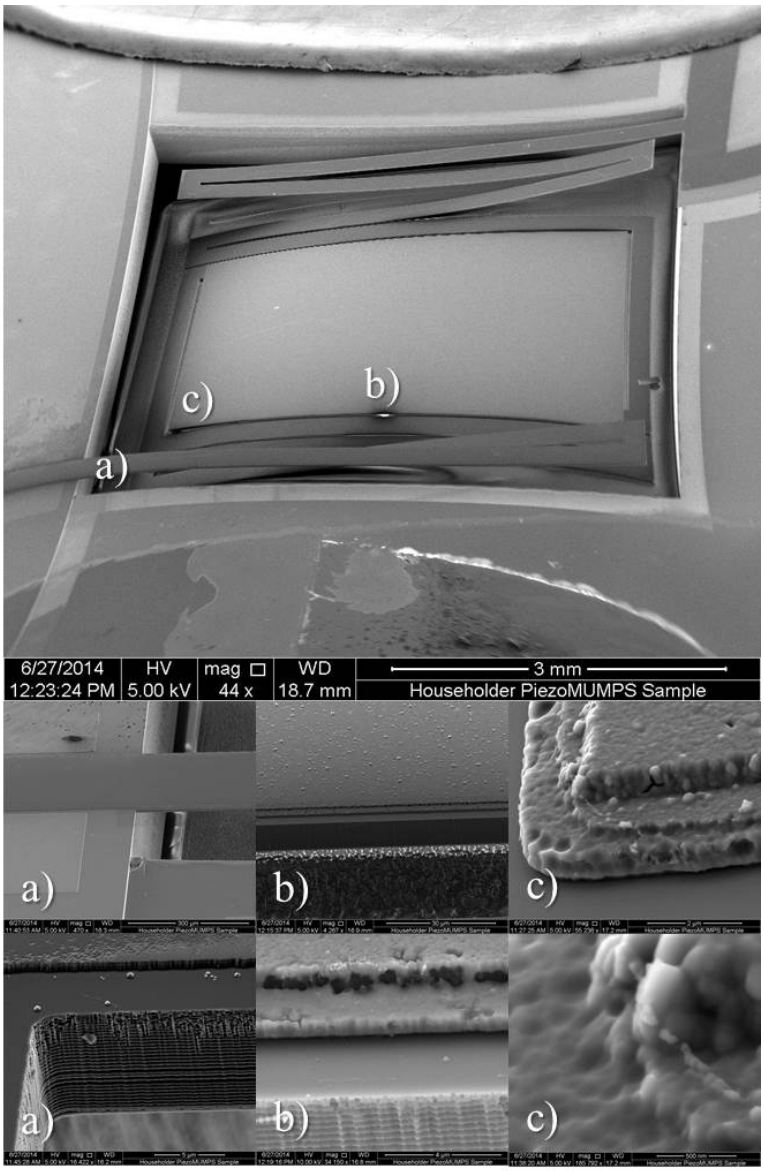

Figure 14. SEM images of second generation PiezoMUMPs device.

B. PHYSICAL AND OPTICAL MEASUREMENTS

Thickness measurements were conducted using the following devices in the Clean Room: KLA D120 Contact Profilometer, a Pro-4 4-point contact probe, Filmetrics spectroscopic thickness measurement instrument, and Zygo NanoView 7100 Optical Profilometer.

The optical profilometer was used to measure the NPS Fabricated on SOI device, shown in Figure 15. The height of the device is uniform across the center pad and its legs, approximately 2.65 µm.

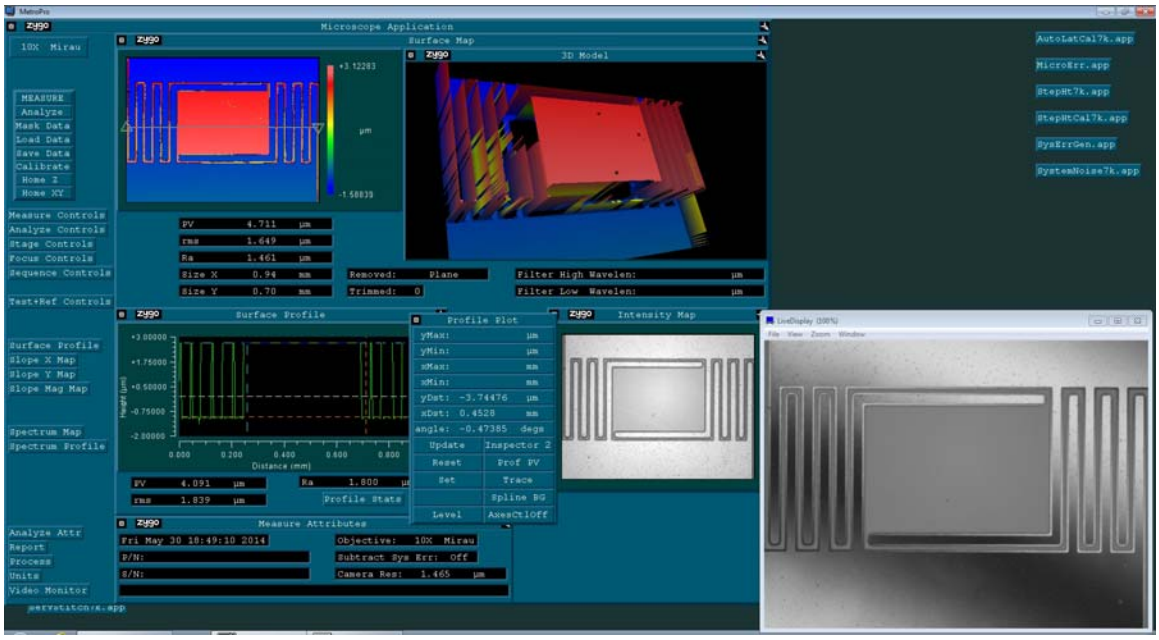

Figure 15. Optical profilometer image of NPS fabricated on SOI device.

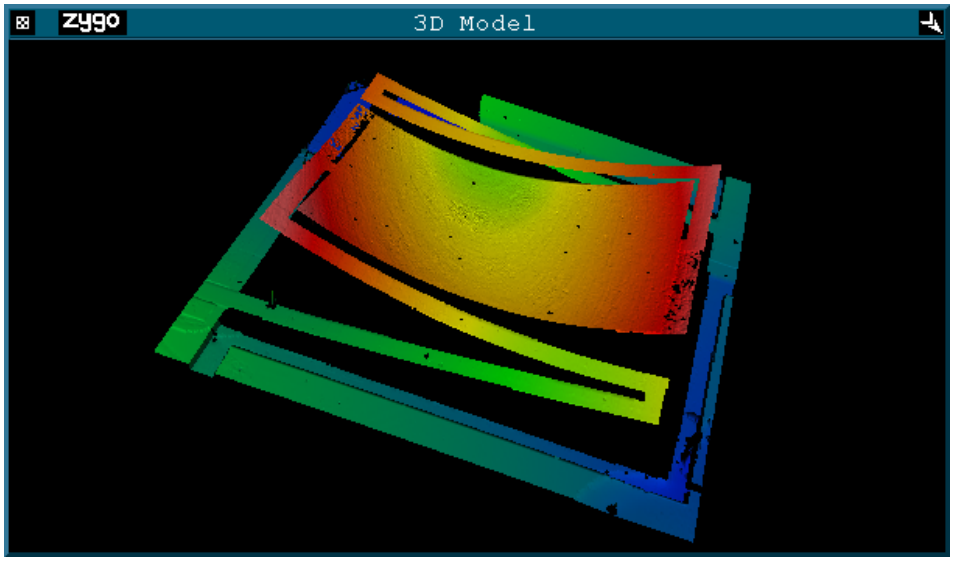

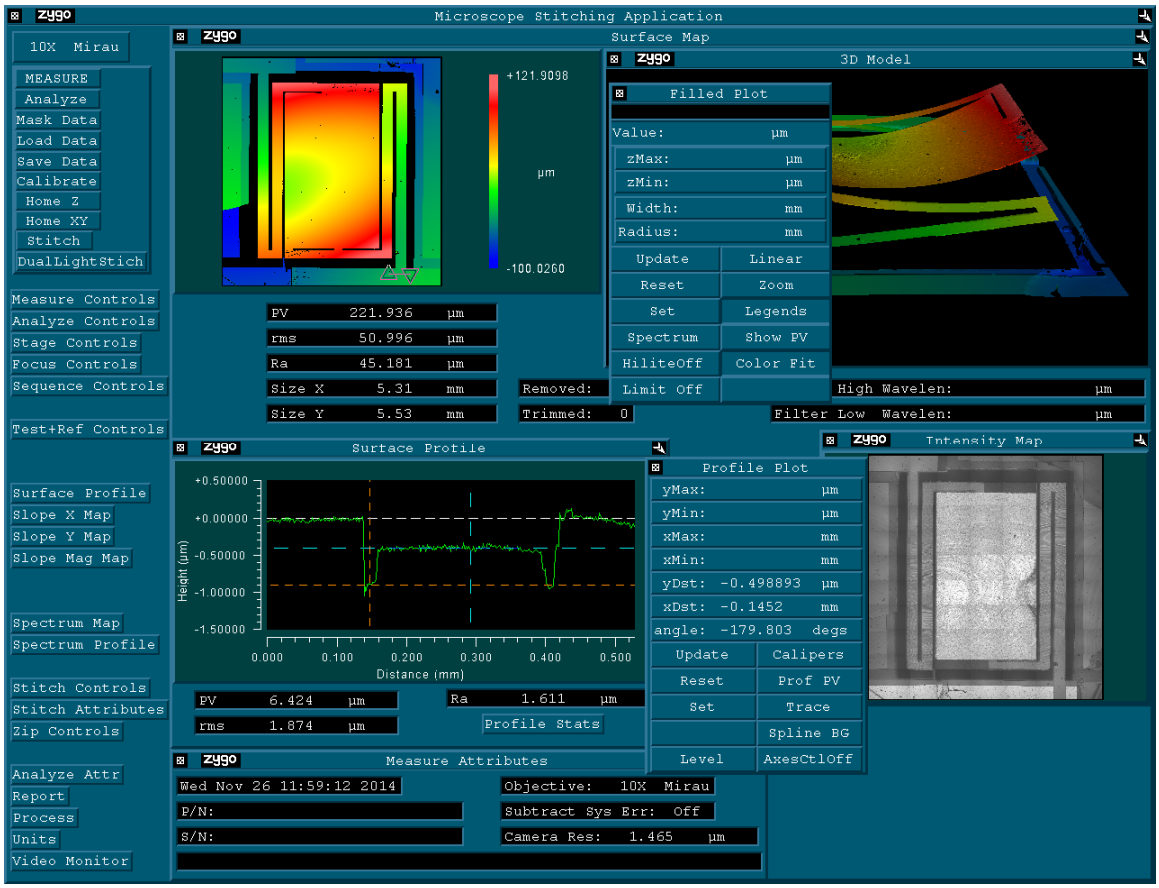

Figure 16. Optical profilometer measurements of device. The curvature of the center pad and legs is expected and is due to residual stress from the microfabrication process. (Note: scale is exaggerated in z direction).

C. LAYER THICKNESS

The best values for use in finite-element analysis were determined above and are listed in Table 3.

Table 3. Device thickness.

	Structure (Si)	Piezo (AlN)	Pad Metal (Al)
Nominal (Design)	10.0 μm	500 nm	1.02 μm
Optical Profilometer	10.1 μm	498.9 nm	0.99 μm
Filmetrics	-	493.2 nm	-
Best Value	10 μm	493 nm	1 μm

D. NANOINDENTER (YOUNG'S MODULUS)

A die with a broken device from the third generation PiezoMUMPs device was analyzed using an Agilent NanoIndenter G200 to find Young's modulus of the Si and the AlN. Young's modulus, or the modulus of elasticity, is a proportionality constant that relates an applied stress to the strain a given material will display in its elastic region. This can be compared to equations (1), (8), and (10), and is often expressed as

$$\sigma = Es \,, \tag{11}$$

where E is Young's modulus (as in equations (8) and (10), not to be mistaken for the induced electric field, E_i in Equation (1)), σ is the stress (S_j in (1)), and s is the strain (T_j in (1)) [5]. Since Young's modulus is the measure of a material's elasticity, it must be as accurate as possible in order to develop computer models that can accurately determine resonance frequency, displacement, and stresses on a device.

The NanoIndenter impresses a triangular diamond tip into a material (see Figure 17) to determine the Young's modulus of bulk material, given Poisson's ratio (v); and of thin films, given the film thickness, Poisson's ratio, and Young's modulus of the substrate. The thin film analysis mathematically removes the expected effect of the substrate on the thin film results. This thesis uses the following values for Poisson's ratio: $v_{Si} = 0.28$ [23], and $v_{AlN} = 0.22$ [24]; and anticipates the following values for Young's modulus: $E_{Si} = 180$ GPa [23], and $E_{AlN} = 331$ GPa [24].

Figure 17. Ten nanoindentations of AlN film.

Using $\nu_{Si} = 0.28$, ten 500 nm deep test points were taken on the silicon layer; one (test #4) was anomalous. Results are shown in Figure 18. After approximately 50 nm the value is consistent and has a very low slope. Averaging the Young's modulus values between 100 nm and 200 nm, the calculated value is $E_{Si} = 173.3$ GPa, with standard error

$$SE_{\text{Sample}} = \frac{s}{\sqrt{n}} = \sqrt{\frac{\sum_{m=1}^{n}\left(E_m - E_{\text{Sample}}\right)^2}{n(n-1)}}, \tag{12}$$

where s is the sample standard deviation, E_m is the value of an individual test, E_{Sample} is the sample's average value, and n is the number of tests. For this run of tests, $SE_{Si} = 0.8$ GPa (roughly 5%).

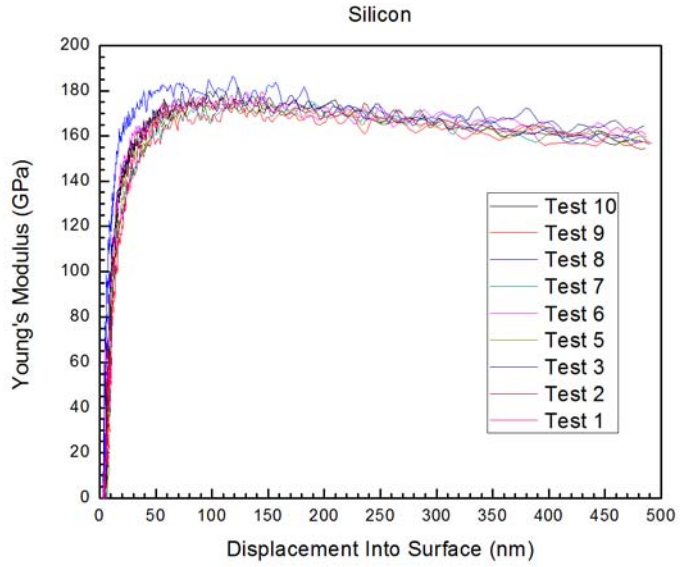

Figure 18. NanoIndenter results for Young's modulus of silicon, 9 of 10 tests. E_{Si} = 173.3 GPa, SE_{Si} = 0.8 GPa.

Using ν_{AlN} = 0.22, film thickness of 493 nm, and substrate (Si) data from above, twenty-four 400 nm deep test points were taken on the aluminum nitride thin film layer; two (test #'s 11 & 16) were anomalous. Results are shown in Figure 19. Above 150 nm the slope becomes flat; however, the variance between individual tests grows substantially after 300 nm. Averaging the Young's modulus values between 35% and 60% of film thickness (173 nm to 296 nm), the calculated value is E_{AlN} = 384.0 GPa, with standard error 3.8 GPa (roughly 10%).

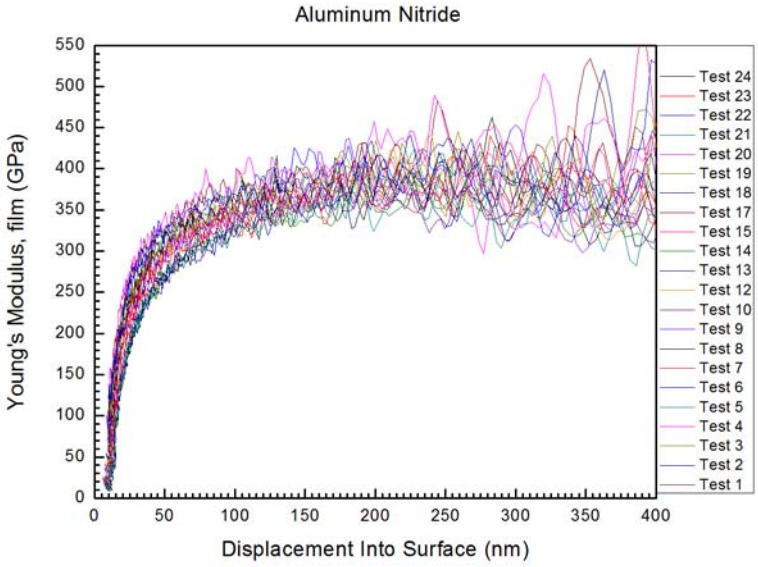

Figure 19. NanoIndenter results for Young's modulus of aluminum nitride, 22 of 24 tests. E_{AlN} = 384.0 GPa, SE_{AlN} = 3.8 GPa.

It should be noted that E_{AlN} has excessive curvature between 50 nm and 100 nm. This is not observed in the E_{Si} data in Figure 18, or in the fused silica reference standard. Though there is greater variance between 50 nm and 100 nm, the reference results are consistent. This implies the low-depth values for AlN represent some kind of surface affect. Further investigation of this phenomenon may improve computer models.

VII. EXPERIMENTAL RESULTS

Experimental results for mechanical parameters, as well as resonance curves in response to the acoustic and mechanical actuation, are used to refine the computer models to enable a more accurate and efficient design process.

A. OUTPUT VOLTAGE MEASUREMENTS

Two basic types of measurements were performed: acoustic and mechanical. Based on the low output voltage, it was necessary to use a Lock-In Amplifier for a majority of the measurements. Further voltage and current measurements would benefit from a low-voltage AC energy harvesting conditioning circuit, such as designed in [25].

1. Acoustic Measurements

An SRS-850 DSP Lock-In Amplifier (LIA) is used to excite a Hewlett Packard 467A Power Amplifier, which drives an HL14-25 Plastic exponential horn (speaker) placed 35^{o} normal to the device; the LIA also monitors and records the root-mean-square voltage (V_{rms}) output from the device. In the acoustic set-up there is a Brüel & Kjær reference microphone with a Type 2670 preamplifier to measure sound pressure in the immediate vicinity of the device; and a Polytec OFV 534 Laser Unit which drives a Mitutoyo model K00232104 laser and is controlled by a Polytec OFV-5000 Vibrometer Controller to measure the maximum displacement of the device. Both the reference microphone and the laser vibrometer use VibSoft 4.7 software for data recording and analysis. This set-up is shown in Figure 20.

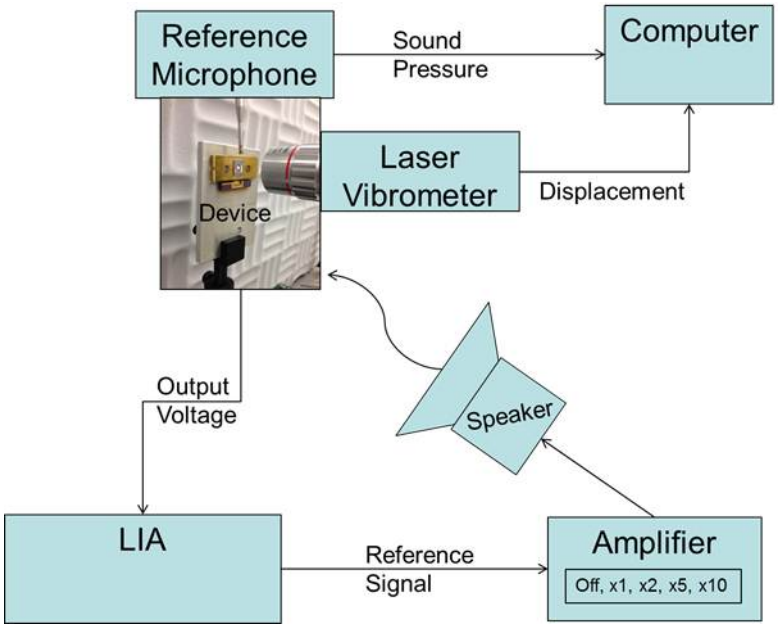

Figure 20. Acoustic test apparatus.

Figure 21 shows the average of Fourier transforms of multiple acoustic sweeps from 100 Hz to 1 kHz. The data are from two independent trials, each an average of 5 sweeps. The peaks apparent at low frequencies are harmonics of 60 Hz. Note the apparent linear response between output voltage and input sound pressure and the seemingly independent displacement peak at 522 Hz.

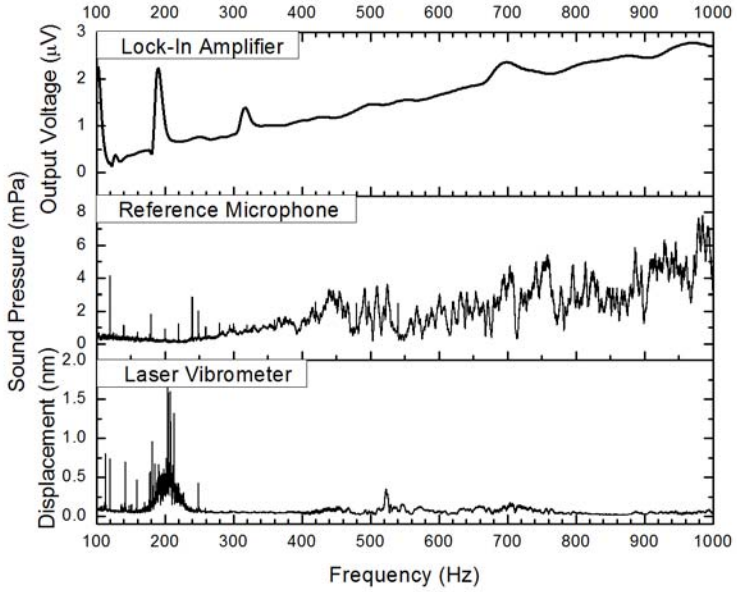

Figure 21. Acoustic trials, average of 10 sweeps over multiple days, 100 Hz to 1 kHz.

Based on the speaker manufacturer's specifications, the reference microphone seems to mirror the expected response curve from the speaker, seen in Figure 22.

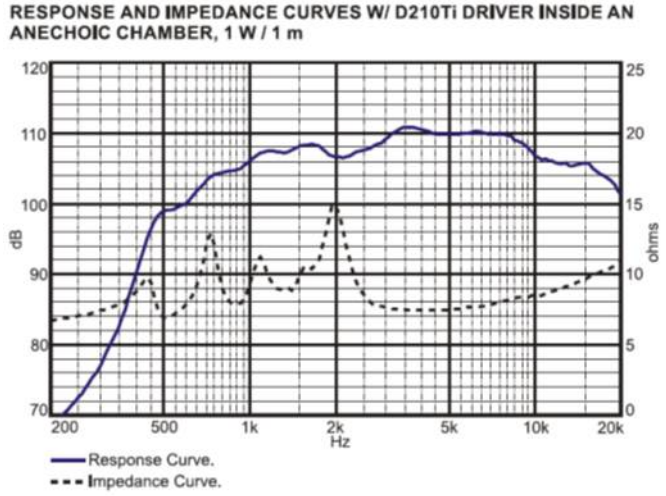

Figure 22. Response and impedance curves for HL14-25 horn, from [26].

a. Response to Varying Incident Amplitude

The adjustable power amplifier between the speaker and the LIA has the following gain settings: OFF, x1, x2, x5, and x10. Figure 23 shows a linear response in output voltage with a change in incident speaker gain. Also note the increasingly stable phase angle as incident speaker gain gets higher.

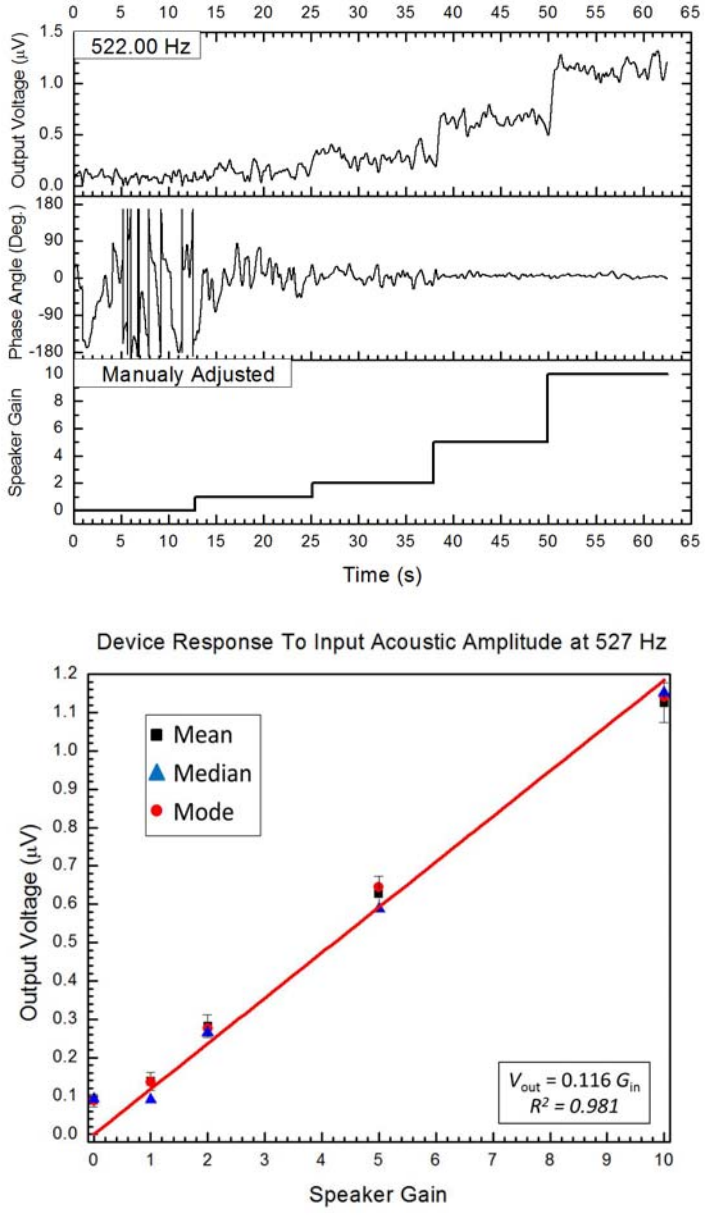

Figure 23. Linear output variation with input gain adjustment.

b. Modal Analysis

The following data was taken from measurements shown in Figure 24. Analysis of this data should be sufficient to determine which resonance mode is the dominant mode excited at each frequency.

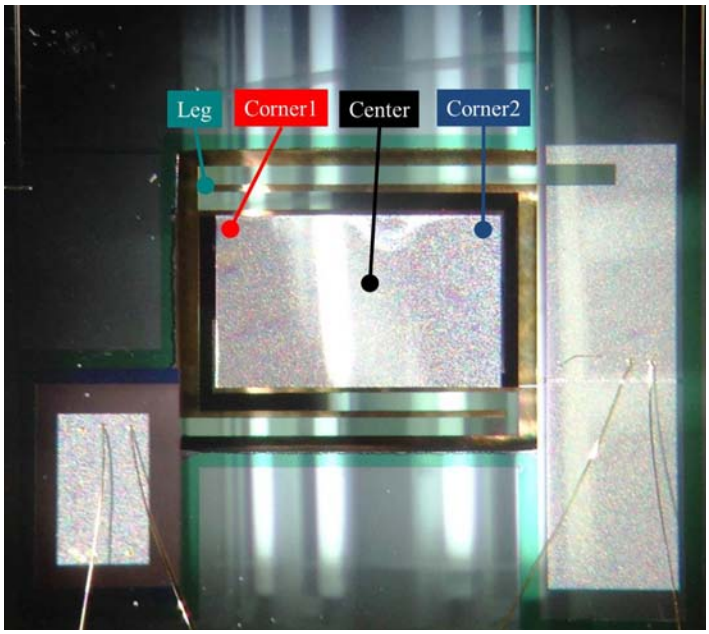

Figure 24. Optical microscope image of PiezoMUMPs third generation device, showing laser vibrometer data locations. Each leg is 250 μm wide.

Figure 25 shows the displacement per unit pressure vs actuating signal frequency obtained during multiple acoustic sweeps from 200 Hz to 900 Hz. The data are averaged from two independent trials, each an average of 10 sweeps. The output plotted is displacement, measured by the laser vibrometer, divided by sound pressure, measured by the reference microphone.

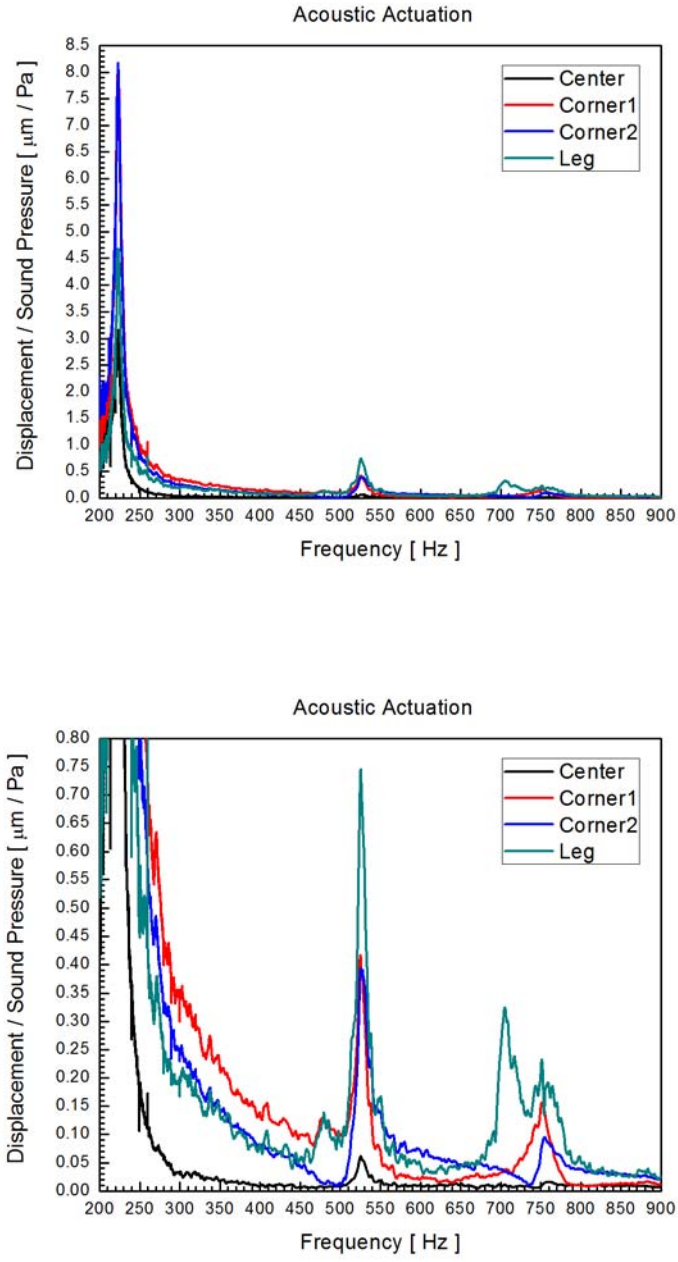

Figure 25. Acoustic trials. Note varying resonance peaks at 220 Hz, 525 Hz, 710 Hz, and 755 Hz and different relative sizes based on location of measurement. The top graph is at full scale to show the 220 Hz peak, the bottom graph is scaled to emphasize the higher-frequency peaks.

Figures 26–28 compare finite-element models to each of the observed peaks from Figure 25. The COMSOL models clamp the ends of the legs and apply a normal uniform

pressure across the center pad and legs. Note in the measurements that the displacement amplitude at the center consistently measures substantially lower than the displacement amplitudes at any other location across the frequency sweep. For the modal analysis the effect of this center measurement is considered qualitatively. The one seeming discrepancy is in the peaks between 200 Hz and 250 Hz. The likely cause is that the measured 207 Hz (corresponding to COMSOL's 229 Hz) peak has a very low Q, so at 223 Hz (COMSOL's 259 Hz) a combination of both is modes excited, thus the discrepant height of the center measurement around 223 Hz.

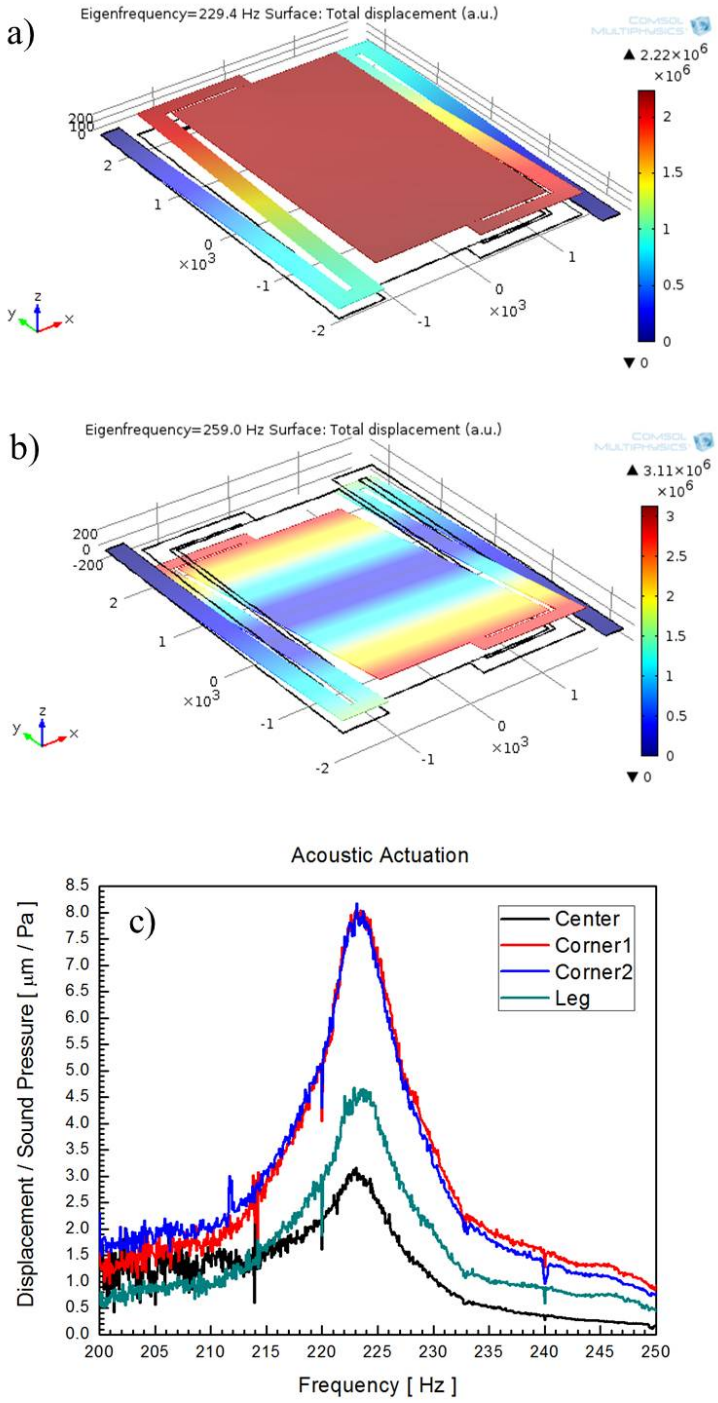

Figure 26. COMSOL deformation shapes for modes at a) 229 Hz and b) 259 Hz, corresponding to c) acoustic peaks observed at 207 Hz and 223 Hz, respectively. Note the corners measure higher than the leg, and the center measures disproportionately higher near 207 Hz.

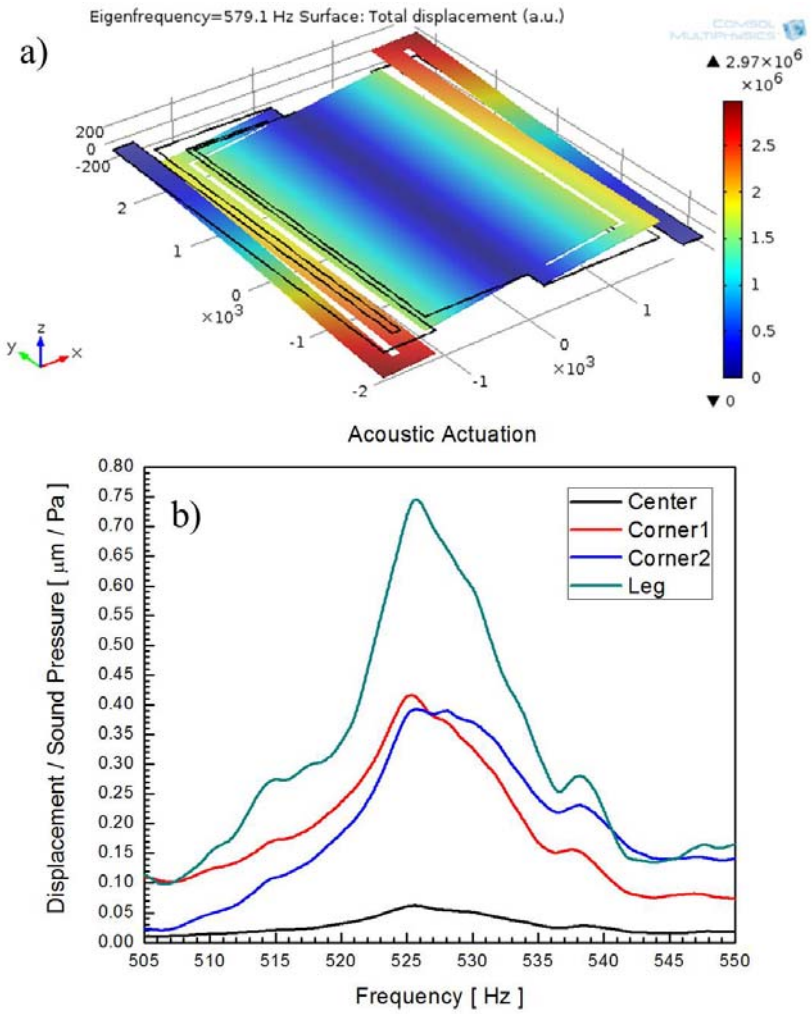

Figure 27. a) COMSOL deformation shape for mode at 579 Hz, corresponding to b) acoustic peak observed at 526 Hz. Note the leg measures highest, the corners somewhat in the middle, and the center barely deflects at all.

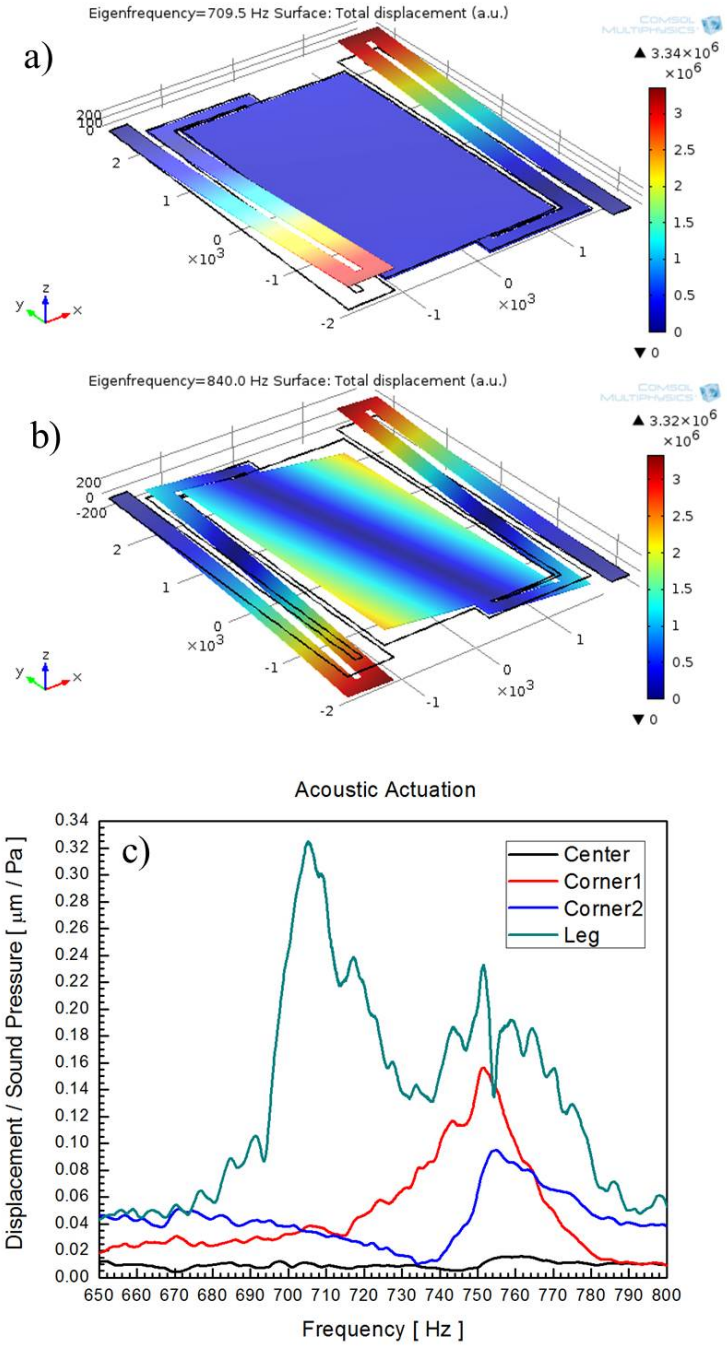

Figure 28. COMSOL deformation shapes for modes at a) 710 Hz and b) 840 Hz, corresponding to c) acoustic peaks observed at 702 Hz and 751 Hz, respectively. Note the leg measures highest, the corners do not deflect at 710 Hz, corner 1 measures higher than corner 2 at 751 Hz, and the center barely deflects at all.

c. Unusual Data

The 223 Hz peak appears to be a linear combination of a high-Q 223 Hz peak with a very low-Q 205 Hz peak, and is seen by the laser vibrometer as independent of acoustic actuation. This is a much noisier signal than the remainder of the Fourier transforms, and its origin remains unknown. An expression analogous to Equation (8) can be used to find that the approximate resonance frequency of the mounting bracket is 20 kHz, and laser vibrometer measurements of the mounting bracket showed little significant displacement near 200 Hz.

The Helmholtz effect was investigated of the mounting bracket that supports the device, where the device substrate acts as a thin neck flange. Viscous penetration depth as a function of frequency is

$$\delta_v = \sqrt{\frac{\eta}{\pi \rho f}}, \tag{13}$$

where η = 2.0x10^{-5} Pa·s, and ρ = 1.2 kg/m^3 are the viscosity and density of air, respectively [27]. At 200 Hz the viscous penetration depth is approximately 150 μm, making the larger gap around the outer rim of the device (between the legs and the substrate) the only effective area of the Helmholtz orifice. Helmholtz frequency for a "thin-neck" resonator is

$$f_0 = \frac{c}{2\pi}\sqrt{\frac{A}{(t+\delta)V}}, \tag{14}$$

where c = 343.6 m/s is the speed of sound in air, $A \approx 4\text{x}10^{-6}$ m^2 is the total area of the effective orifice, t = 10.5 μm is the orifice thickness (structure + piezo layers), $V \approx 150\text{x}10^{-9}$ m^3 is the cavity volume, and δ is the "end correction" and is related to the orifice area [27]. Application of these values to Equation (14) shows that, at 200 Hz, the end correction δ would need to be approximately 2 m. This is unlikely.

Further investigation of the cause of this resonance is recommended. Additionally, it should be possible to make a Helmholtz cavity that stimulates a desired flexural mode.

d. Lorentzian Curve-Fitting

Using the above COMSOL results as a guide for frequency and amplitude values, five independent Lorentzian curves were summed and fit to the experimental data using a "least squares" regression:

$$Z_{Lorentz} = Z_{Bias} + \frac{1}{\pi}\sum_{n=1}^{5} \frac{A_n}{\Delta f_n \left[1 + \left(\frac{f - f_n}{\Delta f_n}\right)^2\right]}, \tag{15}$$

where Z is the displacement, normalized to incident sound pressure; A is a scale factor; f_n is the corresponding peak frequency; Δf is a measurement of the Full Width at Half Maximum (FWHM); and Z_{Bias} is an offset introduced to account for background white noise.

The experimental data from each point in Figure 25 was averaged; the resulting fit of multiple Lorentzian peaks to this averaged data is shown in Figure 29 and summarized in Table 4. The quality factor is determined by dividing each peak frequency by its corresponding FWHM.

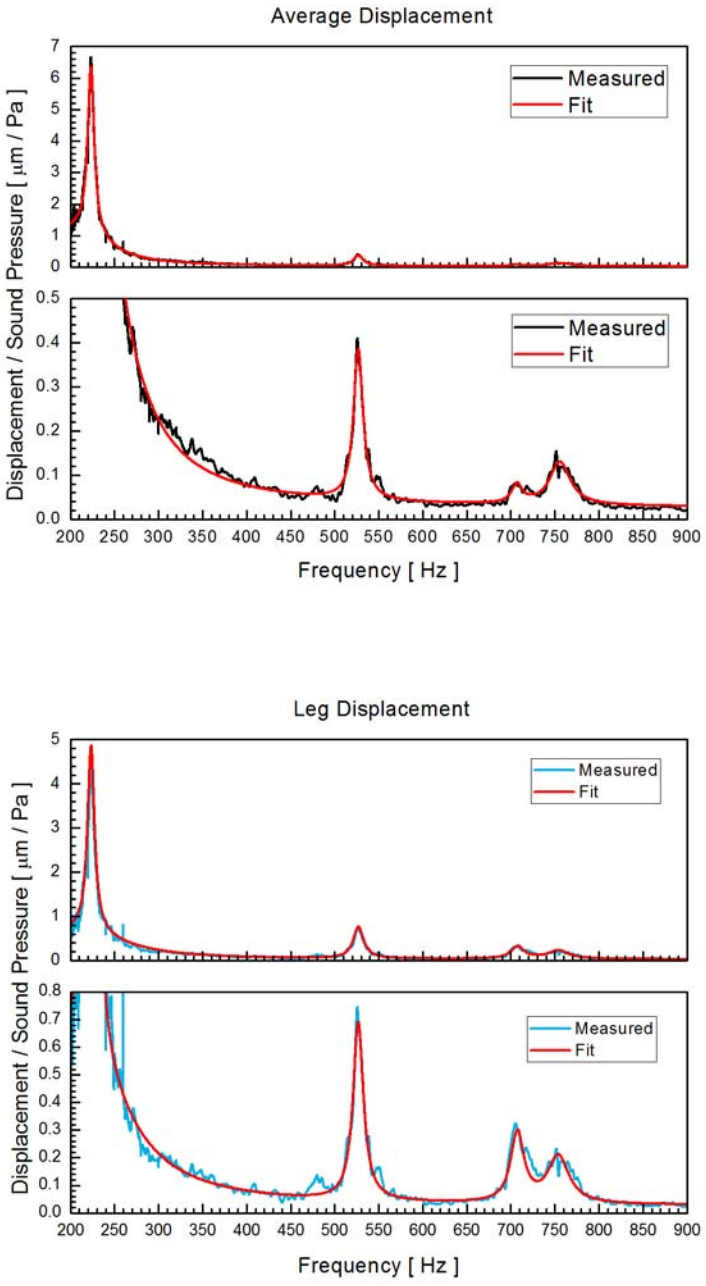

Figure 29. Lorentzian curves fit to acoustically-actuated experimental data averaged over all points (top) and only at the leg (bottom). The top graph in each set is at full scale to show the 220 Hz peak, the bottom graph in each set is scaled to emphasize the higher-frequency peaks.

Table 4. Summary of Lorentzian Fit-to-Leg parameters and modal analysis, with relative displacement color-coded to match COMSOL display.

Measured Freq. (Hz)	Fit f_n (Hz)	Fit Δf (Hz)	Fit Q	Center	Corner 1	Corner 2	Leg	Mode	COMSOL Freq. (Hz)
207	210.0	58.8	3.6	High	High	High	Med	0	229
223.0	223.5	4.76	47.0	Med	High	High	Med	1	259
526.1	526.9	7.16	73.6	Low	Med	Med	High	2	579
705.2	707.5	9.21	76.8	Low	Low	Low	High	3	710
752.2	753.8	14.6	51.7	Low	Med	Low	High	4	840

2. Mechanical Measurements

For the mechanical vibrational measurements, the same Lock-In Amplifier (LIA) and the same energy harvesting device were used. The LIA sends its excitation signal to an Acoustic Power Systems (APS) Model 114 Dual-Mode Power Amplifier, operated in Current Mode for constant force [28], which drives an APS Model 120S Perma-Dyne Shaker. On the shaker, in addition to the device, is an Endevco Isoshear Model 7701A-100 Accelerometer. Both can be either read by the LIA or monitored by a Tektronix DPO 2012 Digital Oscilloscope. The device must be sent through a SRS Model SR560 Low Noise Preamplifier in order to produce a signal that is clean enough to measure on the oscilloscope.

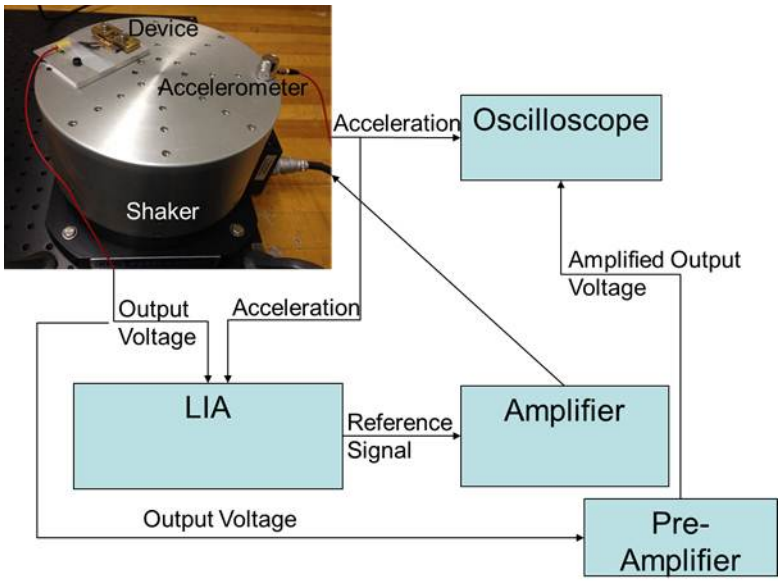

Figure 30. Vibrational test apparatus.

A MotionPro X3 high-speed camera with a Carl Zeiss MAKRO-PLANAR T*, 2-100 mm, ZF.2 macro-lens was used to observe the vibrational mode at 3910 frames per second (see Figure 31). Software analysis of this video will help verify the dominant modes excited.

Figure 31. High speed camera still image of device.

a. Output Voltage

Figure 32 shows multiple resonance peaks, the most dominant at 120 Hz and 380 Hz, and antiresonance peaks at 80 Hz and 360 Hz. An analysis of the accelerometer output shows the apparent peak at 120 Hz is artificial; that is, this harmonic of 60 Hz only shows up due to a dramatic negative spike of the accelerometer output. Equation (16) shows the normalization method in order to factor out the variations of the shaker output.

When necessary, a scale factor is used to match magnitudes to account for minor variations in output.

$$V = \frac{V_{out}}{V_{acc}} \quad , \qquad \theta = \theta_{out} - \theta_{acc} \tag{16}$$

where V_{out} and V_{acc} are the output voltages from the device and the accelerometer, respectively; similarly for phase angle.

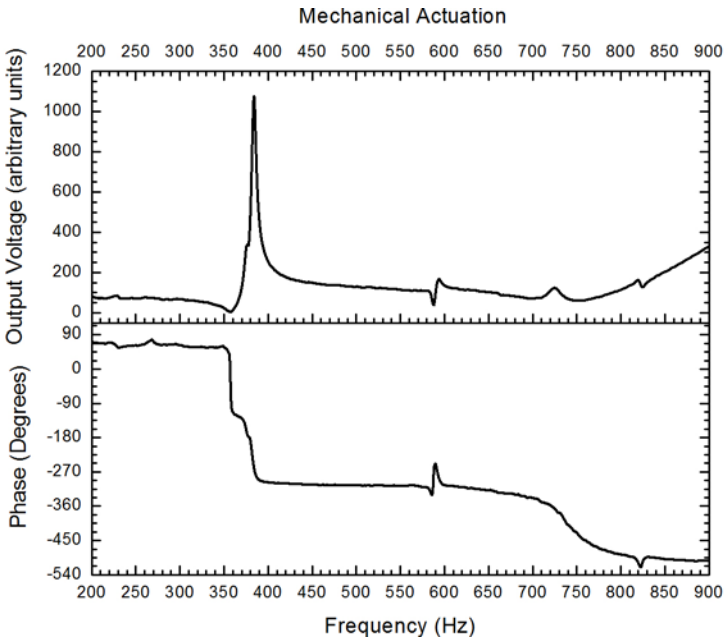

Figure 32. Vibrational sweeps from 200 Hz to 900 Hz, normalized to accelerometer output.

b. Modal Analysis

Due to the difficulty of including the shaker into the acoustic set-up, the mechanical measurements were taken in a different room. This made it impossible to obtain laser vibrometer measurements to perform the same sort of modal analysis as in the acoustic measurements; however, the COMSOL-generated mode shapes for a given acceleration at the leg bases are shown in Figure 33. Note the correlation to peaks observed at 380 Hz and 720 Hz, the only modes where the legs flex in opposite

directions. This suggests that only certain flexural modes will produce a measurable potential difference, and that it is opposite stresses which generate this potential.

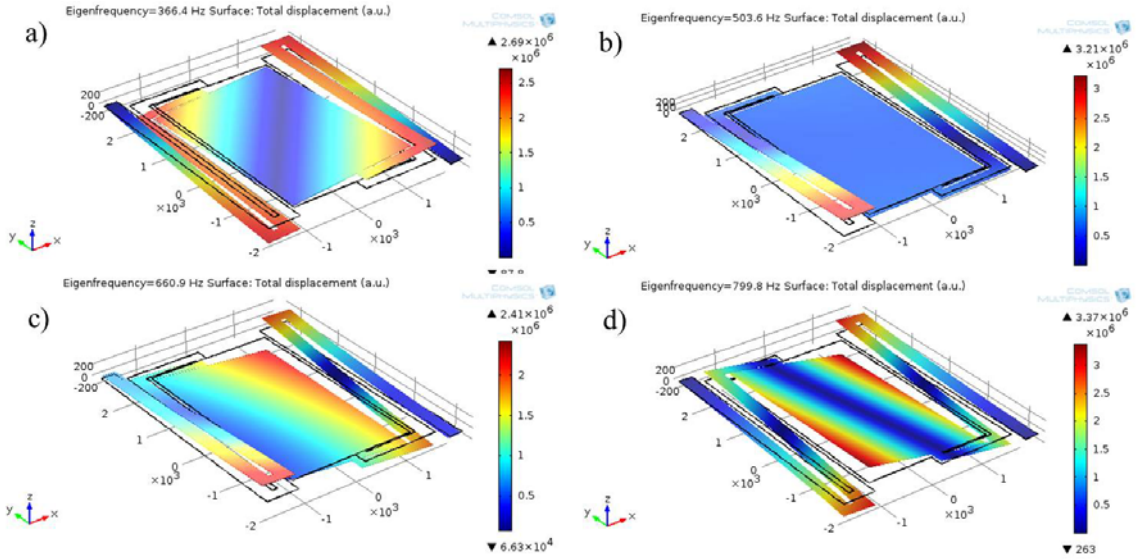

Figure 33. COMSOL mechanically-actuated mode shapes at a) 366 Hz, b) 504 Hz, c) 661 Hz, and d) 800 Hz.

c. Lorentzian Curve-Fitting

A more thorough analysis of the resonance peak at 380 Hz shows an excellent Lorentzian fit, with a high quality factor (Q), as shown in Figure 34. Two independent measurements and a Lorentzian fit are reflected in this plot. The oscilloscope data was measured at discrete points, while maintaining the accelerometer voltage constant at 200 mV_{rms}. The LIA data was normalized to the accelerometer output, as above, and then scaled using a "least squares" regression to match the amplitude of the oscilloscope data. The Lorentzian was then fit to the LIA data using a "least-squares" regression, from 377 Hz – 390 Hz, ignoring the irregularity at low frequencies.

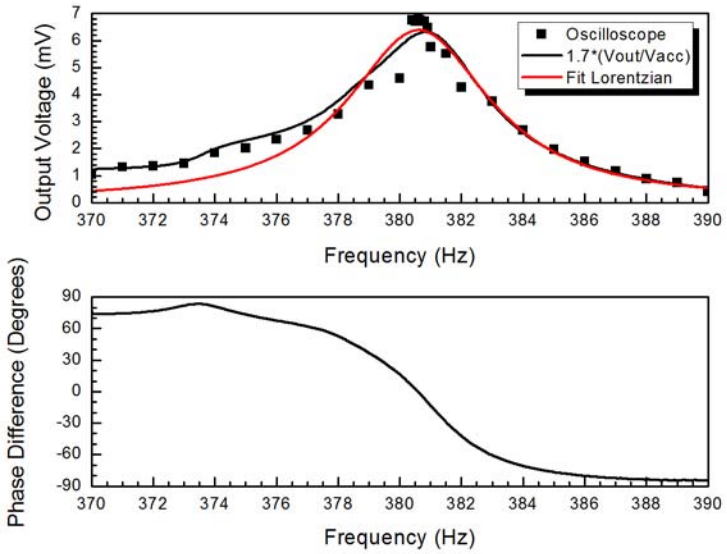

Figure 34. Comparison of scaled LIA data, Oscilloscope data, and best-fit Lorentzian at 380 Hz (top); showing phase shift on LIA (bottom).

Using this fit data, $Q_{Lorentzian}$ can be determined. $Q'_{Lorentzian}$ uses parameters from the best fit Lorentzian over the entire frequency range of 370 Hz to 390 Hz, vice ignoring the irregular data at the low frequency, and provides the most conservative estimate of Q.

$$Q'_{Lorentzian} = \frac{f}{\Delta f} = \frac{380.329}{3.588} = 106.0$$

$$Q_{LIA} = \frac{f}{f_+ - f_-} = \frac{380.861}{382.314 - 378.908} = 111.8 \tag{17}$$

$$Q_{Lorentzian} = \frac{f}{\Delta f} = \frac{380.621}{2.829} = 134.5.$$

The 380 Hz peak is not an artifact of the shaker or accelerometer: first, since we normalized our output data for the shaker's acceleration (meaning actuating force); second, since the shaker's acceleration response levels out after approximately 33 Hz, as

shown in Figure 35 and the accelerometer has an approximately linear deviation (< 2%) from 10–1000 Hz, as shown in Figure 36.

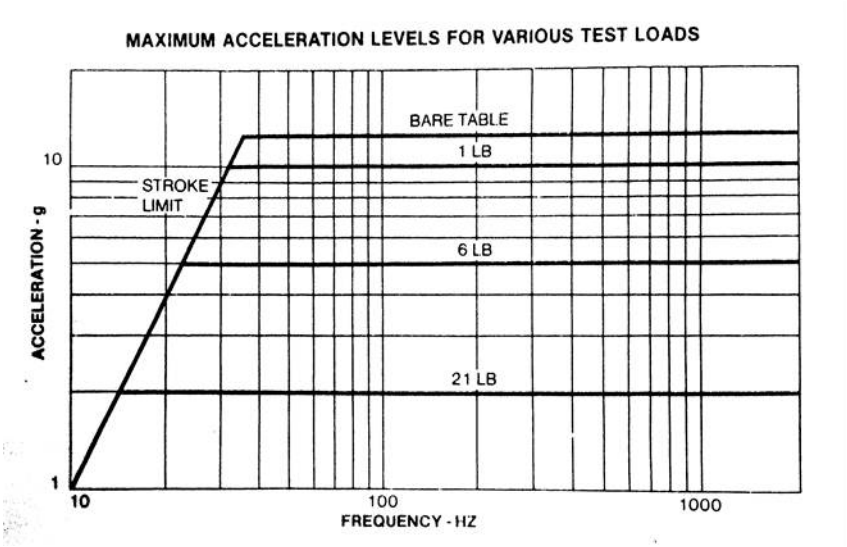

Figure 35. Acceleration performance of shaker under various test loads, from [29].

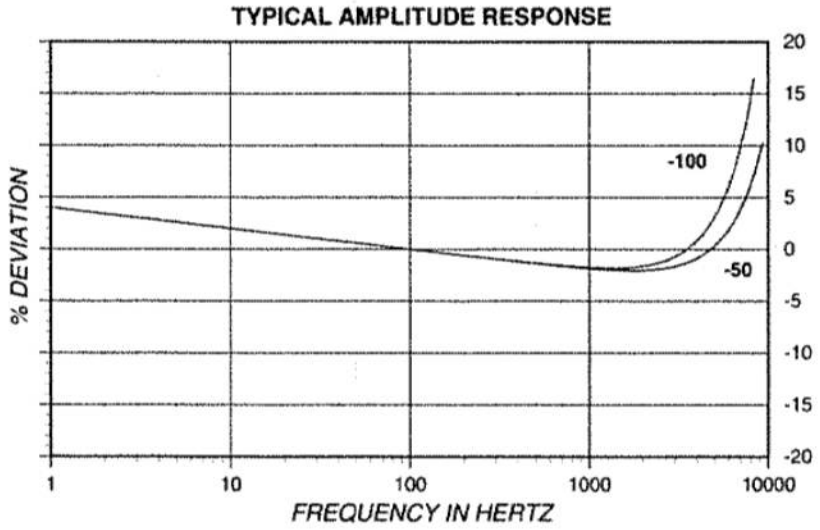

Figure 36. Amplitude response for accelerometer, from [30].

3. Comparison of Acoustic and Mechanical Actuation

Distinctly different vibrational modes stimulated by acoustic vice mechanical excitation are apparent from these measurements. Due to experimental constraints, some possible causes were not investigated; however, slight mechanical excitation in the acoustic set-up allows for some direct comparison. A Fourier transform of two-minutes of mechanical agitation of the acoustic experimental setup is shown in Figure 37. Note the 223 Hz peak is approximately 5x larger in this data, but does not seem to show up when actuated by the shaker.

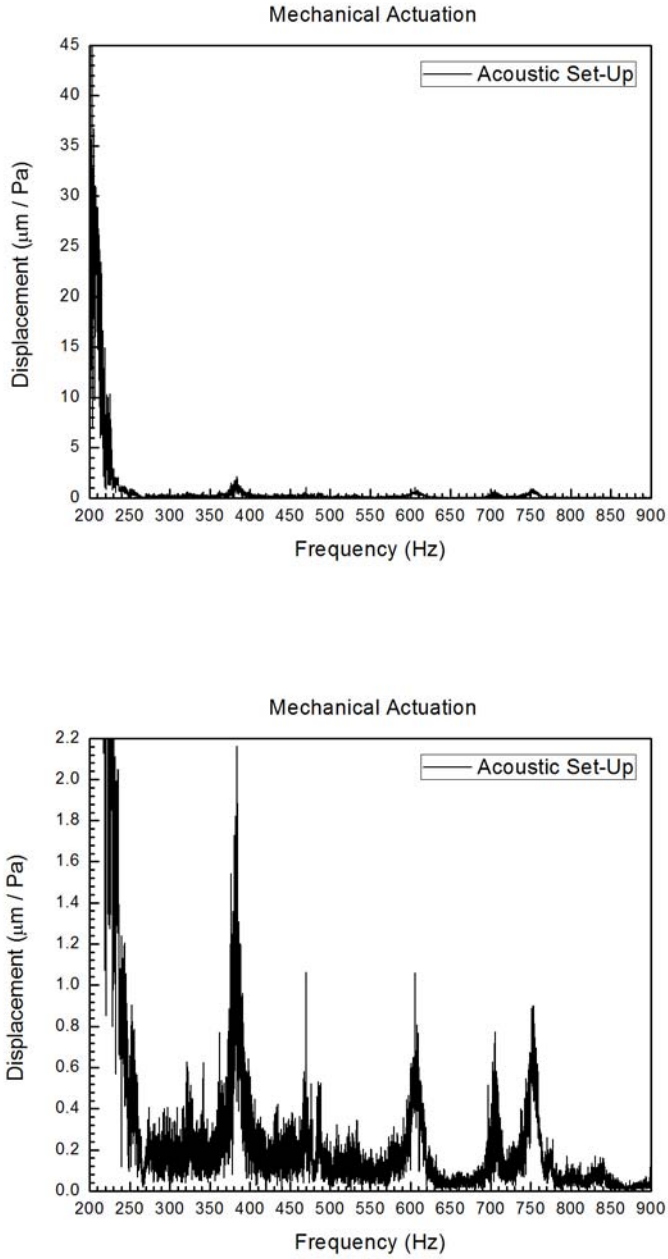

Figure 37. Mechanical excitation in the acoustic experimental set-up. The top graph is at full scale to show the 220 Hz peak, the bottom graph is scaled to emphasize the higher-frequency peaks.

Figure 38 shows a comparison of this data to the voltage data collected from excitation using the mechanical (shaker) set-up. Note the similarity between

corresponding peaks and phase shifts at 380 Hz, 600 Hz, and approximately 700 Hz. Also note the 380 Hz and 600 Hz peaks were not present in the acoustic trials.

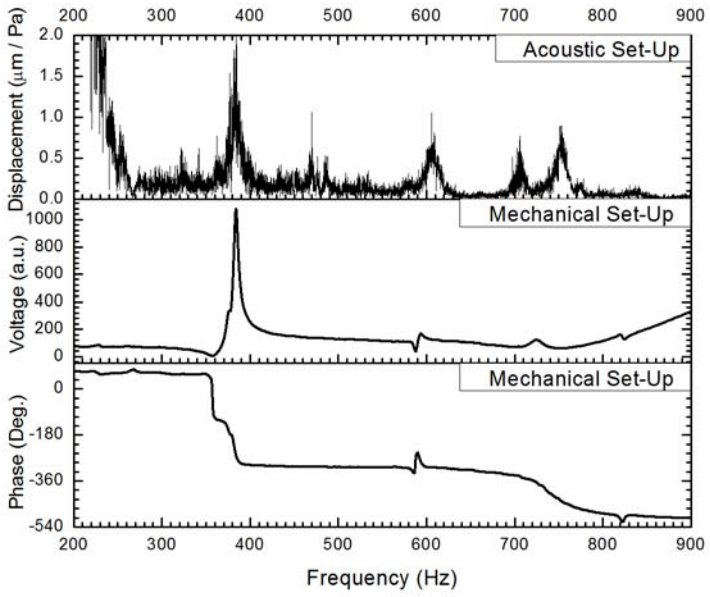

Figure 38. Comparison of mechanical actuation in the mechanical and acoustic experimental set-ups. The measuring point in the acoustic set-up is the device's legs and has been smoothed for clarity of comparison.

The COMSOL-generated mode shapes are repeated in Figures 39 and 40. With the exception of the 229 Hz mode, the shapes are similar (but not identical) to the mechanically-actuated mode shapes. It is likely the 600 Hz and 840 Hz anomalies in the shaker data is due to 60 Hz harmonics, so the only correlating modes are at 380 Hz and across the two 700 Hz peaks, corresponding to opposite leg motion. There is too much noise in the laser vibrometer data to perform mode shape analysis similar to the acoustic trials.

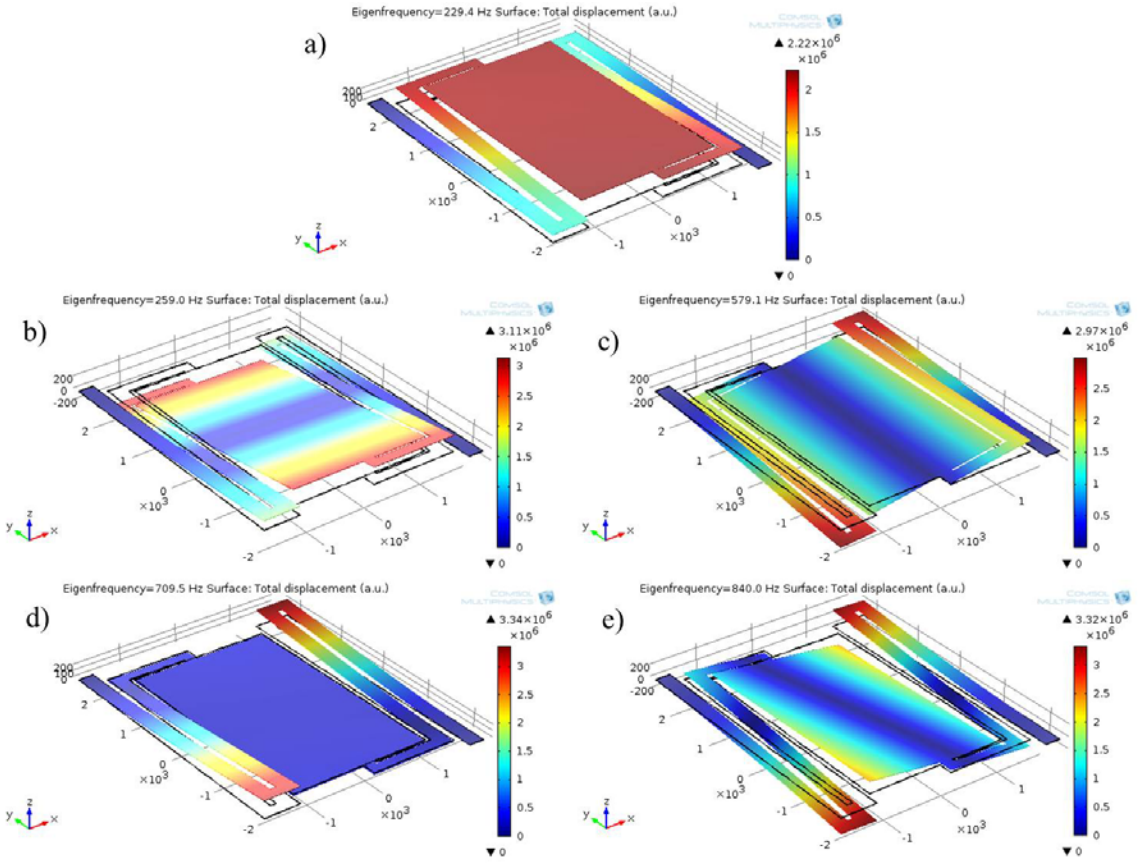

Figure 39. COMSOL acoustically-actuated mode shapes at a) 229 Hz, b) 259 Hz, c) 579 Hz, d) 710 Hz, and e) 840 Hz.

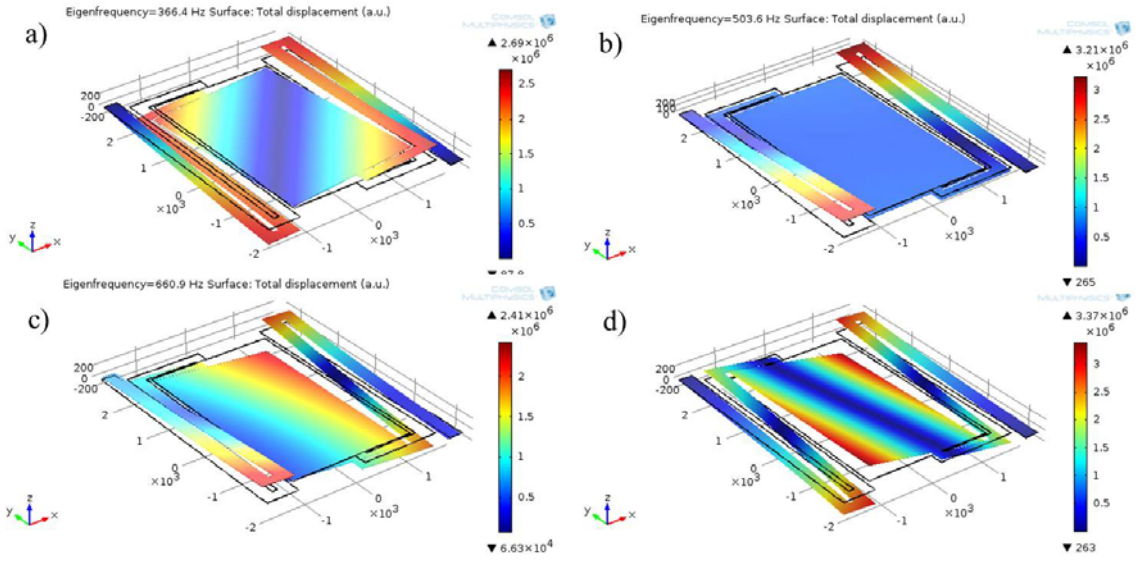

Figure 40. COMSOL mechanically-actuated mode shapes at a) 366 Hz, b) 504 Hz, c) 661 Hz, and d) 800 Hz.

There are only two reliable peaks shown on the voltage measurements of the mechanically actuated device, 381 Hz and 723 Hz. A comparison of Figures 38 and 39 show the corresponding COMSOL modes at 366 Hz and 800 Hz have legs flexing in the opposite directions. Since the connecting pads are configured to take the electric potential from the top of one leg and the bottom of the other, opposite stresses are necessary to generate a potential difference. Since the acoustic set-up measures leg displacement, rather than output voltage, additional peaks are detected for modes that do not produce a potential difference.

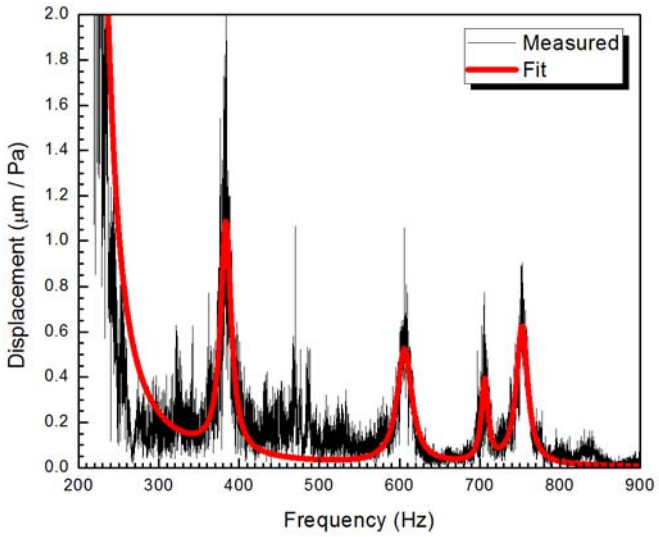

Figure 41. Lorentzian curves fit to vibrationally-actuated experimental data.

The Lorentzian parameters for these fit curves are listed in Table 5.

Table 5. Summary of fit Lorentzian parameters.

Measured Freq. (Hz)	Fit f_n (Hz)	Δf (Hz)	Q	Mode	COMSOL Freq. (Hz)
203	205.5	8.9	23.0	-	-
383	383.6	7.9	48.4	0	366
606	606.2	10.9	55.4	1	504
707	706.2	7.2	98.7	2	661
753	752.9	8.1	92.6	3	800

B. ESTIMATE OF DAMPING PARAMETERS

Rayleigh damping is commonly used in finite-element analysis and provides a convenient method to correlate the measured quality factor to damping due to the mass and stiffness matrices. The damping ratio, ξ_n, is related its corresponding eigenfrequency, ω_n,

$$\xi_n = \left(\frac{1}{2\omega_n}\right)\mathrm{a}_0 + \left(\frac{\omega_n}{2}\right)\mathrm{a}_1, \tag{18}$$

where a_0 and a_1 are the mass and stiffness damping parameters, respectively. MEMS devices traditionally have low damping. In this case the damping ratio is related to Q [31]:

$$\xi_n \approx \frac{1}{2Q_n}. \tag{19}$$

Equating (18) to (19) and fitting the resultant equation to the data in Table 6, initial trial damping parameters were determined to be $a_0 = 22.9\ s^{-1}$, and $a_1 = 2.03\text{x}10^{-6}$ s.

Table 6. Lorentzian parameters used to fit initial Rayleigh damping parameters, taken from the Lorentzian curve fitting of the acoustic data.

Mode	1	2	3	4
f_n	223.4	526.9	706.9	755.6
Q_n	50.2	81.2	97.5	53.1

C. COMPARISON OF SIMULATION AND MEASUREMENTS

Finite Element Modeling is a useful technique for computer modeling. A smooth, continuous system can be divided into a finite number of discrete elements, each with its own set of differential equations. These elements share boundary conditions, and the software numerically evaluates the overall problem.

Since there was no experimental data for basis, the COMSOL finite element models developed in [1] used generic, bulk material values for Young's modulus and Poisson's ratio, as well as selected damping parameters somewhat arbitrarily. These models are further refined, and the results described in Chapters VI and VII are fed back into the models to achieve matching results. The COMSOL models can now be used to design the next-generation devices.

1. Eigenfrequency

More careful and systematic selection of material parameters provides for a more realistic model. The most important values that determine eigenfrequencies are Young's modulus and Poisson's ratio, as they describe the elastic deformation of a material. Using the more accurate measured values, the COMSOL generated eigenfrequencies are listed in Table 7.

Table 7. Eigenfrequencies generated by finite element modeling.

Actuation Method	Frequency (Hz)				
Center Pad (incident pressure)	229	259	579	710	840
Anchor (prescribed acceleration)	-	366	504	661	800

2. Damping

Using the damping parameters calculated above, a frequency domain sweep was conducted in COMSOL, shown in Figures 42. Note the peaks are starting to appear divided at 220 Hz and 710 Hz, similar to the experimental data.

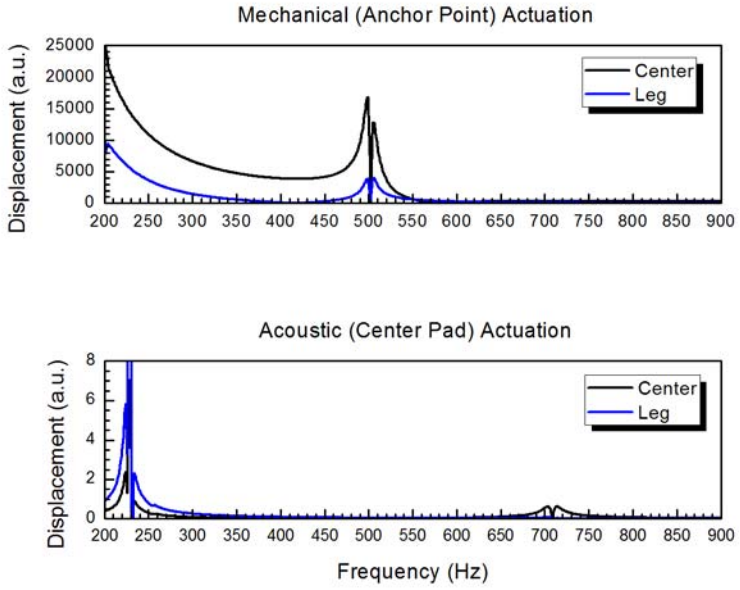

Figure 42. COMSOL frequency domain sweep 200 Hz - 900 Hz for center-pad (top) and anchor-point (bottom) actuation, in increments of 1 Hz, using the above damping parameters.

The parameters entered into COMSOL for analysis in this thesis are compared to the original values and listed in Table 8.

Table 8. Summary of COMSOL input parameters.

	Young's Modulus – Si (GPa)	Poisson's Ratio – Si	Young's Modulus – AlN (GPa)	Poisson's Ratio – AlN	a_0 (s^{-1})	a_1 (s)
Original	170	0.28	344	0.22	1	$2x10^{-8}$
Updated	173.3	0.28	384.0	0.22	22.9	$2.03x10^{-6}$

D. ESTIMATE OF POWER AND EFFICIENCY

The LIA has an input resistance of 50 MΩ with a 25 pF capacitance, and the oscilloscope has input resistance of 1 MΩ with 11.5 pF capacitance. Since capacitive reactance is

$$X_C = \frac{1}{2\pi fC}, \tag{20}$$

the LIA values range from 63.7 MΩ at 100 Hz to 6.37 MΩ at 1 kHz, and oscilloscope values range from 13.8 MΩ to 138 MΩ. This provides an input impedance range of the LIA for the frequencies analyzed in this thesis of 50.4 MΩ to 81.0 MΩ, and oscilloscope impedance range from 13.8 MΩ to 138 MΩ.

The maximum measured steady state voltage at resonance frequency is 6.8 mV_{p-p} = 4.8 mV_{rms} at 380.5 Hz on the oscilloscope and 220.8 μV_{rms} at 379.3 Hz on the LIA. The oscilloscope has input impedance of 36.4 MΩ and the LIA has input impedance of 52.7 MΩ at their respective frequencies. This means the device is providing $P = V^2/R$ = 0.633 pW to the oscilloscope and 0.924 fW to the LIA. Note the large difference in power output for the different monitoring devices. This superficially agrees with finite element models from [1], that there can be several orders of magnitude difference in power output depending on load impedance.

Of note, these values are power delivered to equipment that is designed not to draw much power. Matching impedances using a circuit such as designed in [25] will

enable an increase in power produced per device of several additional orders of magnitude. A summary of this estimation is below in Table 9.

Table 9. Power delivered by one device.

	Voltage (mV_{rms})	Frequency (Hz)	Impedance (MΩ)	Power (fW)
Oscilloscope	4.8	380.5	36.4	633.0
Lock-In Amplifier	0.221	379.3	52.7	0.924

THIS PAGE INTENTIONALLY LEFT BLANK

VIII. FUTURE WORK

Most of the Future Work recommendations from [1] and [25] remain valid. These include refinement of the microfabrication process and analysis of combinations of conditioning circuitry for multiple devices. Further recommendations are listed below.

A. MODELING

With the data obtained in chapters VI and VII, more detailed and accurate computer models can be obtained. These models can then be used to design better, more optimal devices.

1. Exploring the Parameter Space

There are several parameters that would benefit from further analysis, and more accurate matching of finite-element models to experimental values. Eigenfrequency and modal matching, as well as quality factor matching, are the most important of them.

Comparison of the high-speed video described in Chapter VII, and of additional videos at other frequencies, to COMSOL-generated mode shapes will enable confirmation of the dominant modes excited by mechanical stimulation. Further investigation of laser vibrometer results at various locations on the device and their comparison to COMSOL mode shapes will also enable confirmation of the dominant modes excited by acoustic stimulation.

Continued analysis of material (Young's modulus and Poisson's ratio, for example) and damping parameters (mass and structural damping) is necessary to further match finite-element models with experimental results. More realistic and reliable computer models can then be used to test future generations without requiring as much experimental validation. This will significantly reduce the timeline and the cost of design.

2. Next Generation Devices

Other than the obvious adjustments of leg and center pad dimensions and geometry, the next generation devices could be improved by determining the points of

highest potential difference and laying the electrode pads across the equipotential surfaces. One option is to cover the top of the entire piezo layer with a single Al pad metal layer and connect the bottom of each piezo leg together with another pad metal layer to obtain the highest possible current for the "top-to-bottom" potential difference.

B. FABRICATION

The ability to deposit alternative structure layers and piezo layers at NPS will greatly reduce the cost of each MEMS device.

1. NPS Fabrication with SOI and SU-8

With the Bosch deep reactive ion etch instrument fully functional, it is now possible to finish microfabrication of the designs intended for NPS fabrication. Final refinement of the fabrication process and analysis of SU-8 as a structure layer will be necessary, as listed below.

a. Fabrication

- Determine the Bosch etching parameters for backside trenching to free a suspended device.

b. SU-8 Analysis

- Determine experimental data for deposited SU-8, such as Young's modulus, hardness, and Poisson's ratio to update computer simulations.
- Determine eigenfrequencies of each multileg structure and compare to computer simulations.
- Determine resilience of SU-8 structures, both long-term cyclic fatigue and one-time failure.

2. NPS Deposition of AlN

- Continue analysis of reactive sputtering AlN at NPS.
- Investigate other options for deposition of AlN, such as reactive ion impregnation with a plasma etcher.

C. TESTING

Initial testing of a single device was conducted in this thesis. More extensive testing is necessary to refine finite-element modeling parameters to input into COMSOL.

1. Conditioning Circuit

Since the power output from each device is a function of the load, determining output impedance of each device is necessary to design the optimum conditioning circuit. Very little modification to the circuitry designed in [25] will be required for this purpose.

2. Multiple Device Arrays

Since different resonance modes will generate outputs with different phases, it is possible that the optimal arrangement of multiple devices will differ based on the dominant mode excited. An in-depth analysis of output waveforms in conjunction with utilization of the conditioning circuit above will provide the first steps toward developing an array of MEMS vibration and acoustic energy harvesters that can provide usable power.

3. Power and Efficiency Analysis

Updated COMSOL data will enable better estimates of the output power and efficiency of individual devices and of arrays of devices, which can be compared to measured values. Following this determination, a Ragone plot showing power density vs. energy density will allow a convenient comparison to other energy harvesting devices.

4. Failure Analysis

The device analyzed in Chapter VII has been subjected to several hours of use with no discernable change in behavior. MEMS devices are characteristically robust; however, a deeper understanding of the effective lifetime of any device can be extraordinarily helpful.

A small selection from each design must be subjected to extreme conditions for failure analysis, and the rest must be tracked over their lifetime to monitor fatigue. Useful

information to track would be the effect of numerous cycles, normalized to acceleration or pressure, on eigenfrequency values and peak displacement and output voltage.

5. Investigating Unusual Findings

During Young's modulus determination unusual data was discovered on the surface (50 nm–100 nm) of the AlN layer. Further analysis of the surface of the AlN layer will help build even more accurate computer models.

A resonance peak between 200 Hz and 250 Hz was detected, even without incident sound, during the acoustic trials. COMSOL models predict the two lowest resonance frequencies to be near this value. Investigation into the cause of this peak will lead to a better understanding of the MEMS device and its effects.

D. MODAL ANALYSIS

The only resonance frequency that seems to overlap between experiments using acoustic and mechanical actuation is between 700 Hz and 750 Hz. The COMSOL-generated mode shapes at 840 Hz (acoustic) and 800 Hz (mechanical) are very similar.

1. Center-Pad versus Anchor-Point Actuation

The resonance frequencies are different, both in value and in mode shape, for different methods of actuation. Analysis of the differing effective masses for each method of actuation will enable understanding of this phenomenon.

2. Helmholtz Resonance

Voltage is generated when the device legs flex in opposite directions. According to COMSOL this occurs at 259 Hz, 579 Hz, and 840 Hz for center-pad (acoustic) actuation; and at 366 Hz and 800 Hz for anchor-point (mechanical) actuation. Experiment shows a possible voltage peak near 700 Hz for acoustic actuation. It should be possible to design a cavity that stimulates this resonance frequency to enable harvesting of ambient acoustic energy.

LIST OF REFERENCES

[1] D. Hogue and S. Gregory, "MEMS-based waste vibrational energy harvesters," M.S. thesis, Dept. Physics, Naval Postgraduate School, Monterey, CA, 2013.

[2] Executive Office of the President, "The president's climate action plan," The White House, Washington, DC, 2013.

[3] Deputy Secretary of Defense, "Deputy's management action group guidance for a comprehensive defense energy policy," Department of Defense, Washington, DC, 2013.

[4] Deputy Commandant for Combat Development and Integration, "Marine Corps Science & Technology Strategic Plan," Washington, DC, 2012.

[5] C. Liu, *Foundations of MEMS.* Upper Saddle River, NJ: Prentice Hall, 2012.

[6] C. D. Richards, M. J. Anderson, D. F. Bahr and R. F. Richards, "Efficiency of energy conversion for devices containing a piezoelectric component," *J Micromech Microengineering,* vol. 14, pp. 717, 2004.

[7] S. O. Kasap, *Principles of Electronic Materials and Devices.* New Delhi, India: McGraw Hill, 2012.

[8] U.S. Navy, Gas turbine systems technical (electrical) / gas turbine systems technical (mechanical) 3, volume 2," NAVEDTRA 14114, Pensacola, FL: Naval Education and Training Professional Development and Technology Center, 1991.

[9] PiezoMUMPs. (n.d.). MEMSCap. [Online]. Available: http://www.memscap.com/products/mumps/piezomumps. Accessed Nov. 6, 2014.

[10] SU-8 permanent photoresists table of properties. (n.d.). MicroChem. [Online]. Available: http://www.microchem.com/pdf/SU-8-table-of-properties.pdf. Accessed Nov. 19, 2014.

[11] SU-8: thick photo-resist for MEMS. (2013, Dec.). *MEMScyclopedia*. [Online]. Available: http://memscyclopedia.org/su8.html. Accessed Nov. 19, 2014.

[12] I. Ivanov, L. Hultman, K. Järrendahl, P. Mårtensson, J. Sundgren, B. Hjörvarsson and J. Greene, "Growth of epitaxial AlN (0001) on Si (111) by reactive magnetron sputter deposition," *J. Appl. Phys.,* vol. 78, pp. 5721–5726, 1995.

[13] W. Meng, J. Heremans and Y. Cheng, "Epitaxial growth of aluminum nitride on Si (111) by reactive sputtering," *Appl. Phys. Lett.,* vol. 59, pp. 2097–2099, 1991.

[14] S. Saravanan, E. Berenschot, G. Krijnen and M. Elwenspoek, "A novel surface micromachining process to fabricate AlN unimorph suspensions and its application for RF resonators," *Sensors and Actuators A: Physical,* vol. 130, pp. 340–345, 2006.

[15] A. Ababneh, U. Schmid, J. Hernando, J. Sánchez-Rojas and H. Seidel, "The influence of sputter deposition parameters on piezoelectric and mechanical properties of AlN thin films," *Materials Science and Engineering: B,* vol. 172, pp. 253–258, 2010.

[16] H. Cheng, Y. Sun, J. Zhang, Y. Zhang, S. Yuan and P. Hing, "AlN films deposited under various nitrogen concentrations by RF reactive sputtering," *J. Cryst. Growth,* vol. 254, pp. 46–54, 2003.

[17] J. H. Choi, J. Y. Lee and J. H. Kim, "Phase evolution in aluminum nitride thin films on Si (100) prepared by radio frequency magnetron sputtering," *Thin Solid Films,* vol. 384, pp. 166–172, 2001.

[18] E. Iborra, J. Olivares, M. Clement, L. Vergara, A. Sanz-Hervás and J. Sangrador, "Piezoelectric properties and residual stress of sputtered AlN thin films for MEMS applications," *Sensors and Actuators A: Physical,* vol. 115, pp. 501–507, 2004.

[19] J. Zhang, H. Cheng, Y. Chen, A. Uddin, S. Yuan, S. Geng and S. Zhang, "Growth of AlN films on Si (100) and Si (111) substrates by reactive magnetron sputtering," *Surface and Coatings Technology,* vol. 198, pp. 68–73, 2005.

[20] M. Morita, T. Ohmi, E. Hasegawa, M. Kawakami and K. Suma. Control factor of native oxide growth on silicon in air or in ultrapure water. *Appl. Phys. Lett. 55(6),* pp. 562–564. 1989. DOI: http://dx.doi.org/10.1063/1.102435.

[21] K. Wafers and C. Misra, "Oxides and hydroxides of aluminum," Alcoa Labs., Tech. Rep. 19, 1987.

[22] A. Cowen, G. Hames, K. Glukh and B. Hardy, "PiezoMUMPs design handbook, rev. 1.0," MEMSCAP Inc, 2012.

[23] M. A. Hopcroft, W. D. Nix and T. W. Kenny, "What is the Young's Modulus of Silicon?" *Microelectromechanical Systems, Journal Of,* vol. 19, pp. 229–238, 2010.

[24] Properties of Typical Aluminum Nitride Substrates. (2014). Valley Design Corp. [Online]. Available: http://www.edgepolishing.com/aluminum-nitride.htm. Accessed Oct. 30, 2014.

[25] D. Shvets, "Analysis of AC low-voltage energy harvesting," M.S. thesis, Dept. Elect. Eng., NPS, Monterey, CA, 2014.

[26] HL14-25 Spec Sheet. (2005, Nov.). Selenium. [Online]. Available: http://www.jblpro.com/ProductAttachments/HL14-25_SpecSheet.pdf. Accessed Nov. 14, 2014.

[27] L. E. Kinsler, A. R. Frey, A. B. Coppens and J. V. Sanders, *Fundamentals of Acoustics*. Hoboken, NJ: John Wiley & Sons, 2000.

[28] *Dual mode model 114 amplifier*, Acoustic Power Systems, Carlsbad, CA, n.d.

[29] *Perma-dyne model 120S shaker*, Acoustic Power Systems, Carlsbad, CA, n.d.

[30] ENDEVCO, "ISOSHEAR model 7701A-100 peizoelectric accelerometer data sheet," San Juan Capistrano, CA, n.d.

[31] J. F. Semblat, "Rheological interpretation of Rayleigh damping," *J. Sound Vibrat.,* vol. 206, pp. 741–744, Oct. 1997. DOI: http://dx.doi.org/10.1006/jsvi.1997.1067.

THIS PAGE INTENTIONALLY LEFT BLANK

INITIAL DISTRIBUTION LIST

1. Defense Technical Information Center
   Ft. Belvoir, Virginia

2. Dudley Knox Library
   Naval Postgraduate School
   Monterey, California